

# Joint Metrics for EMF Exposure and Coverage in Real-World Homogeneous and Inhomogeneous Cellular Networks

Quentin Gontier, *Student Member, IEEE*, Charles Wiame, *Student Member, IEEE*, Shanshan Wang, *Member, IEEE*, Marco Di Renzo, *Fellow, IEEE*, Joe Wiat, *Senior Member, IEEE*, François Horlin, *Member, IEEE*, Christo Tsigros, Claude Oestges, *Fellow, IEEE*, and Philippe De Doncker, *Member, IEEE*

**Abstract**—This paper evaluates the downlink performance of cellular networks in terms of coverage and electromagnetic field (EMF) exposure, in the framework of stochastic geometry. The model is constructed based on datasets for sub-6 GHz macro cellular networks but it is general enough to be applicable to millimeter-wave networks as well. On the one hand, performance metrics are calculated for  $\beta$ -Ginibre point processes which are shown to faithfully model a large number of motion-invariant networks. On the other hand, performance metrics are derived for inhomogeneous Poisson point processes with a radial intensity measure, which are shown to be a good approximation for motion-variant networks. For both cases, joint and marginal distributions of the EMF exposure and the coverage, and the first moments of the EMF exposure are provided and validated by Monte Carlo simulations using realistic sets of parameters from two sub-6 GHz macro urban cellular networks, i.e., 5G NR 2100 (Paris, France) and LTE 1800 (Brussels, Belgium) datasets. In addition, this paper includes the analysis of the impact of the network parameters and discusses the achievable trade-off between coverage and EMF exposure.

**Index Terms**— $\beta$ -Ginibre point process, coverage, dynamic beamforming, EMF exposure, inhomogeneous Poisson point process, Nakagami- $m$  fading, stochastic geometry.

## I. INTRODUCTION

TELECOMMUNICATION operators are faced with the challenge of optimizing the coverage of their cellular networks while ensuring compliance with public electromagnetic field (EMF) exposure limits. On the one hand, the study of coverage, outage, data rate or spectral efficiency can be carried

out through the evaluation of the signal-to-interference-and-noise ratio (SINR). On the other hand, the EMF exposure is subject to restrictions for public health reasons specified in terms of incident power density (IPD), or, equivalently, in terms of electric field strength [1], [2]. However, both metrics are still most often considered independently even though their correlation is high and their combination is necessary to fully address network optimization problems. Both also heavily depend on the randomness in the network topology. To capture this aspect, stochastic geometry (SG) theory can be efficiently employed as an alternative to numerical simulations. Using this framework, base stations (BSs) are modeled as spatial point processes (PPs) [3], [4], for which closed-form expressions characterizing the average network performance can be derived. Motivated by these considerations, **the main aim of this paper is to introduce a mathematical framework, applicable to real-world networks, for jointly evaluating the trade-offs between SINR and EMF exposure to electromagnetic fields for both motion-invariant, i.e. both stationary (translation invariant) and isotropic (rotation invariant) networks, and motion-variant networks.**

### A. Related Works

1) *Evaluation of the SINR by using SG*: The SINR was the initial metric explored within the SG framework [5]. Regular hexagonal lattices [6] or perfect square lattices [7] were the first models of cellular networks being considered. They were embedded in the SG framework because they are extreme cases for modeling the repulsion between the points of a PP. These models are often limited to simulations because of their lack of mathematical tractability. Another body of studies [3], [8], [9] employed the homogeneous Poisson point process (H-PPP), consisting of randomly located points in the region of interest, without any spatial dependence between them. Although the H-PPP leads to highly tractable analytical expressions, which explains its use in most of the SG literature applied to telecommunication networks, it cannot model spatial repulsive or attractive behaviors between points. Numerical results have shown that H-PPPs provide a lower bound for the coverage probability of real cellular networks while hexagonal lattices provide an upper bound [10]. In another body of works, more advanced PP models are investigated (e.g., Strauss Hardcore PP [11], Grey Saturation PP [11], Poisson

Q. Gontier, F. Horlin and Ph. De Doncker are with Université Libre de Bruxelles, OPERA-WCG, Avenue F.D. Roosevelt 50 CP 165/81, 1050 Brussels, Belgium (quentin.gontier@ulb.be). C. Wiame and C. Oestges are with ICTEAM Institute, Université Catholique de Louvain, 1348 Louvain-la-Neuve, Belgium. S. Wang and J. Wiat are with LTI, Telecom Paris, Chaire C2M, Institut Polytechnique de Paris, Palaiseau, France. M. Di Renzo is with Université Paris-Saclay, CNRS, CentraleSupélec, Laboratoire des Signaux et Systèmes, 3 Rue Joliot-Curie, 91192 Gif-sur-Yvette, France (marco.di-renzo@universite-paris-saclay.fr). C. Tsigros is with Département Technologies et Rayonnement, Brussels Environnement, Belgium. The work of Q. Gontier was supported by Innoviris under the Stochastic Geometry Modeling of Public Exposure to EMF (STOEMP-EMF) grant.

The work of M. Di Renzo was supported in part by the European Commission through the Horizon Europe project titled COVER under grant agreement number 101086228, the Horizon Europe project titled UNITE under grant agreement number 101129618, and the Horizon Europe project titled INSTINCT under grant agreement number 101139161, as well as by the Agence Nationale de la Recherche (ANR) through the France 2030 project titled ANR-PEPR Networks of the Future under grant agreement NF-Founds 22-PEFT-0010, and the ANR-CHISTERA project titled PASSIONATE under grant agreement ANR-23-CHR4-0003-01.

Hard-core process [12]). A complete taxonomy of PP models frequently used in the literature of cellular networks can be found in [13]. Some models lead to tractable expressions but have not been tested in real-world networks [12], [14]. Other models have been validated in real-world networks but the analytical expressions are highly intractable mathematically: approximations are usually required to obtain mathematical expressions for useful performance metrics [11], [15]–[18]. Finally, some studies provide models addressing tractability and accuracy aspects, but they are only applicable to motion-invariant networks [19], [20]. This is for example the case of  $\beta$ -Ginibre point processes ( $\beta$ -GPPs) which allow for tractable and accurate modeling of many motion-invariant networks, as shown for the city of Paris, France, in [21] and for thirteen networks in Western Europe in [22]. Previous analyses for  $\beta$ -GPP cellular networks are however limited to the SINR cumulative distribution function (CDF) [23], [24]. Regarding motion-variant networks, the literature is very scarce. Inhomogeneous Poisson point processes (I-PPPs) models have been widely used in the literature, but only to replace equivalent more complex motion-invariant PPs, from the point of view of the typical user for downlink (DL) analyses [19] or from the point of view of the typical BS for uplink (UL) analyses [25], [26]. These works cannot capture the dependence of the network performance on the location of the user under investigation. The only attempt to derive the SINR complementary cumulative distribution function (CCDF) in an inhomogeneous network is in [27] where the authors consider a generalized PPP setup with an  $\alpha$ -stable distributed BS density (which can be seen as a generalization of the I-PPP), whose parameters are fitted to empirical data but at a cost of analytical tractability.

2) *Evaluation of the IPD by using SG:* More recently, the IPD has progressively gained interest in the SG community to evaluate the performance of wireless power transfer systems [28], [29], with the objective to estimate the amount of power that can be harvested in the context of the Internet-of-Things. In [30], the energy correlation is investigated in a wireless power transfer system where the transmitters use dynamic beamforming (BF). The evaluation of the IPD to assess the EMF exposure for public health concerns is more recent. Indeed, the IPD and EMF exposure are highly coupled since the objective of EMF-aware systems is to ensure that the incident power is low enough to fulfill exposure thresholds. In the SG context, a first attempt to model the EMF exposure can be found in [2]. The authors use an empirical propagation model for a 5G massive multiple-input multiple-output (mMIMO) network in the millimeter wave (mmWave) band. In [1], the theoretical distribution of the EMF exposure is compared to an experimental distribution obtained from measurements in an urban environment. This model is then used in [31] to study BS densification scenarios. It is worth mentioning that numerous works employed deterministic models to evaluate the impact of network densification on the EMF exposure [32], [33]. The EMF exposure has also been numerically assessed in an indoor environment in [34], by using a methodology akin to the SG framework. This involves obtaining a large number of ray-launching realizations by employing a randomized arrangement of scatterers for each realization. In the context

of SG modeling, the EMF exposure is analyzed considering a max-min fairness power control in a 5G mMIMO network in [35]. At last, the EMF exposure is analyzed in networks where sub-6 GHz and mmWave BSs coexist in [36]. It is worth noting that all works characterizing the IPD represent the network topology by relying on a H-PPP, which cannot capture the spatial repulsions and attractions that characterize general network deployments.

3) *Joint evaluation of the IPD and SINR by using SG:* In the context of energy harvesting, SG brought a new perspective to simultaneous wireless information and power transfer (SWIPT) analyses by allowing the computation of the joint CCDF in order to find a trade-off between coverage and harvested power. These studies take into account many features including line-of-sight and non-line-of-sight links, time switching and power splitting schemes, dynamic BF [37] and mMIMO [38]. Similar tools can be used for a joint analysis of the EMF exposure and the SINR. To the best of the authors' knowledge, the CCDF of the SINR and the CDF of the EMF exposure have been analyzed separately and the only analytical frameworks studying them jointly are reported in [39] for Manhattan networks and [40] for user-centric cell-free mMIMO networks. The DL EMF exposure, the UL EMF exposure caused by the typical user's smartphone and the DL signal-to-noise ratio (SNR) are studied in [41]. However, the authors did not conduct a joint analysis of the EMF exposure and SNR in their study.

## B. Contributions

Motivated by these considerations, the aims of the present paper are (i) to introduce an analytical framework for jointly evaluating the trade-offs between coverage and EMF exposure for two different PPs (motion-invariant and motion-variant) and (ii) to validate the approach by using realistic datasets for sub-6 GHz macro BSs tailored to the large majority of urban and rural environments. The specific contributions of this paper are as follows:

1) *Motion-invariant networks:* For motion-invariant networks, the proposed mathematical approach is based on a  $\beta$ -GPP. The first contribution is to complement the previous analyses described in Subsection I-A1 by developing a framework for calculating mathematical expressions for the following metrics:

- Mean and variance of the EMF exposure;
- Marginal CDF of the EMF exposure;
- Joint CDF of the EMF exposure and SINR.

2) *Motion-variant networks:* The motion-invariant assumption does not hold anymore for cities with a historic city center that is characterized by a high BS deployment density and a lower deployment density as the distance from the city center increases. In these scenarios, in addition, the BS density is often found to be angle-independent. We, therefore, go beyond classical studies applied to motion-invariant networks by introducing an I-PPP model for motion-variant networks, which is characterized by a radial intensity measure. The second contribution is the development of a comprehensive framework

Ref.	Topology						Mathematical performance metrics of interest			
	Spatial repulsion	Motion-variance	Real-world	Tractability	Nakagami- $m$ fading	Dynamic beamforming	SI(N)R CCDF	IPD CCDF	Joint distribution	DL/UL
[1], [2], [31]			✓	✓				✓		DL
[3], [4]			✓	✓						/
[5]				✓			✓			DL
[6], [11]	✓						✓			DL
[7], [18]	✓				✓		✓			DL
[8], [10]			✓				✓			DL
[9]			✓		✓		✓			DL+UL
[12], [14], [23], [24]	✓			✓			✓			DL
[15], [21], [22]	✓		✓	✓						DL
[16], [17]	✓		✓				✓			DL
[19], [20]	✓		✓	✓			✓			DL
[25], [26]							✓			UL
[27]	✓	✓	✓				✓			DL
[28], [29]				✓				✓		DL
[30]				✓	✓	✓				DL
[32], [33]										DL
[34]										UL
[35]				✓						DL
[36]				✓	✓	✓		✓		DL
[37], [38]				✓		✓			✓	DL
[39], [40]	✓			✓			✓	✓	✓	DL
[41]				✓	✓		✓*	✓		DL+UL
This work	✓	✓	✓	✓	✓	✓	✓	✓	✓	DL

TABLE I: Comparison between the relevant literature and this work. \*: Study of the SNR only.

for calculating mathematical expressions in motion-variant networks. In particular, the following metrics are derived:

- Mean and variance of the EMF exposure;
- Marginal CDF of the EMF exposure and marginal CCDF of the SINR;
- Joint CDF of the EMF exposure and SINR.

Finally, the developed frameworks are applied to real-world networks for both the motion-invariant and the motion-variant cases. The network performance is evaluated using realistic system parameters.

A comparison between this work and the most related works is summarized in Table I.

### C. Structure of the Paper

The paper is organized as follows: Section II introduces the network topologies and the system model. Section III provides mathematical expressions for the performance metrics of interest by using SG. Numerical validations based on two real-world network deployments are provided in Section IV. Finally, conclusions are given in Section V.

## II. SYSTEM MODEL

### A. Mathematical Background

Let  $\mathcal{B} \in \mathbb{R}^2$  be the two-dimensional area where the considered network is located. Let  $\Psi = \{X_i\}$  be the PP of BSs in  $\mathcal{B}$ , which are assumed to have the same technology, to belong to the same network provider and to transmit at the same frequency  $f$ .  $\Psi$  is modeled as a realization of a PP of density  $\lambda(u)$ ,  $u \in \mathcal{B}$ .  $\Psi$  is stationary if its statistical properties remain unaffected after any translation. It is isotropic if its statistical properties are invariant under any rotation.  $\Psi$  is called motion-invariant if it is stationary and isotropic.

1) *Motion-Invariant Networks:* In the motion-invariant case, a good estimator of the true BS density  $\lambda$  is the number of BSs within  $\mathcal{B}$  divided by the area of  $\mathcal{B}$ . Motion-invariance implies that the performance metrics are statistically identical at any point in an infinite network. It is a common practice to consider a typical user centered at the origin to facilitate the analysis. In a finite network, it is often assumed that the results do not vary as the typical user stays away from the boundaries of the area  $\mathcal{B}$ .

In Section III, the performance metrics for motion-invariant networks will be derived for  $\beta$ -GPP models, which are characterized by a constant density  $\lambda$  and a parameter  $\beta$ . The  $\beta$  parameter is between 0 and 1 [23], with  $\beta = 0$  corresponding to a H-PPP and  $\beta = 1$  to a Ginibre Point Process (GPP). The main difficulty compared to other PP models comes from the fact that  $\beta$ -GPPs are constructed from GPPs, which are defined from a complex kernel [23]. For these PP models, there exists no analytical probability density function (PDF) of the distance to the nearest BS,  $f_{R_0, \Theta_0}$ . Let  $X_i, i \in \mathbb{N}$  denote the points of a  $\beta$ -GPP with density  $\lambda$ , which is denoted by  $\Phi_\lambda^\beta$ .  $\Phi_\lambda^\beta$  is constructed from the GPP  $\Phi_{\lambda/\beta}^1 = \{X_i\}_{i \in \mathbb{N}}$  with density  $\lambda/\beta$  by independent thinning with probability  $\beta$ . The set of square distances,  $\{|X_i|^2\}_{i \in \mathbb{N}}$ , has the same distribution as  $\{Y_i\}$  such that  $Y_i \sim \text{Gamma}(i, \pi\lambda/\beta)$ ,  $i \in \mathbb{N}$  are mutually independent [24]. This property can be used to derive performance metrics since it is possible to take advantage of the existence of an analytical PDF for the square distance to each BS  $X_i$ . The PDF of  $Y_i$  is given by

$$f_i(u) = \frac{u^{i-1} e^{-\frac{cu}{\beta}} (c/\beta)^i}{(i-1)!} \quad (1)$$

with  $c = \lambda\pi$ . To obtain  $\Phi_\lambda^\beta$  from  $\Phi_{\lambda/\beta}^1$ , each element of  $\Phi_\lambda^\beta$  is associated with a mark  $\xi$ . Then,  $\{\xi_i\}_{i \in \mathbb{N}}$  is the set of marks of  $\Phi_{\lambda/\beta}^1$ , which are mutually independent and identically distributed random variables with  $\mathbb{P}(\xi_i = 1) = \beta$

and  $\mathbb{P}(\xi_i = 0) = 1 - \beta$ . Accordingly, the serving BS denoted by  $X_0$  is  $X_i$  if  $\xi_i = 1$  and if all the other BSs are located farther than  $X_i$ , i.e.  $\{X_0 = X_i\} = \{\xi_i = 1\} \cap \mathcal{A}_i$  where  $\mathcal{A}_i = \{\xi_j = 1, |X_j| > |X_i|\} \cup \{\xi_j = 0\} \forall j \in \mathbb{N} \setminus \{i\}$ .

2) *Motion-Variant Networks*: If  $\Psi$  is motion-variant, an inhomogeneous PP model needs to be selected. Unfortunately, inhomogeneous models are intractable mathematically, except for the I-PPP, which can be viewed as an approximation of some more complex models. The computations of performance metrics then require the use of a spatially-varying density function  $\lambda(u), u \in \mathcal{B}$ , which is fitted to the empirical BS density by, e.g., using a least-square method.

Large European cities are often characterized by the presence of a densely populated historic center, with old buildings and an irregular street organization, leading to a high density of BSs to accommodate the large data traffic. As the distance from the city center increases, the density of antennas decreases, leading to an almost radial density [22]. Based on these considerations, a flexible radial density model is chosen, which is monotonically decreasing with  $\rho$  and is characterized by 6 parameters  $\tilde{a}, \tilde{b}, \tilde{c}, \tilde{d}, \tilde{\rho}, \tilde{\theta}$ :

$$\lambda(\rho, \theta) = \frac{\tilde{a}}{\Delta(\rho, \theta)} + \tilde{b} + \tilde{c}\Delta(\rho, \theta) + \tilde{d}(\Delta(\rho, \theta))^2 \quad (2)$$

with  $\Delta^2(\rho, \theta) = \tilde{\rho}^2 + \rho^2 - 2\tilde{\rho}\rho \cos(\theta - \tilde{\theta})$ . The user is located at the origin of the coordinate system. The 4 parameters  $\tilde{a}, \tilde{b}, \tilde{c}, \tilde{d}$  must be chosen so that the conditions  $\lambda(\rho, \theta) \geq 0$  and  $\partial\lambda/\partial\Delta \leq 0$  are met for  $\rho \leq \tau$  where  $\tau$  is the radius of the disk centered at the origin inside which the network is studied and can take arbitrary large or infinite values. For this choice of parameters,  $(\tilde{\rho}, \tilde{\theta})$  is the point of maximal BS density.

The mathematical tractability of the performance metrics increases if the intensity measure

$$\Lambda(\mathcal{D}) = \int_{\mathcal{D}} \lambda(u) du, \quad (3)$$

where  $\mathcal{D} \in \mathcal{B}$ , is purely radial, which is the case analyzed here. The mathematical expressions derived for motion-variant networks in this paper are only valid for the typical user located at the origin of the coordinate system but, as shown in Subsection IV-B1, they can be calculated at other user locations through a change of coordinate system so that the user is located at the center of this new coordinate system. Practically speaking, the approach consists of replacing  $\lambda(u)$  by  $\lambda(u - u_C)$  in all the expressions, where  $u_C$  is the point of interest in the old coordinate system.

## B. Propagation Model

The propagation model is defined as

$$P_{r,i} = P_t G_i G_r |h_i|^2 l_i \quad (4)$$

where  $P_{r,i}$  is the received power from BS  $X_i$ ,  $P_t$  is the transmit power of  $X_i$ ,  $G_i$  is the gain of  $X_i$  in the direction of the user,  $G_r$  is the gain of the receiver, assumed isotropic and equal to 1 to simplify the analysis,  $|h_i|^2$  accounts for the fading and  $l_i = l(X_i) = \kappa^{-1} (r_i^2 + z^2)^{-\alpha/2}$  is the path loss attenuation with exponent  $\alpha > 2$ ,  $\kappa = (4\pi f/c_0)^2$  where  $c_0$  is the speed of light,  $r_i$  is the distance between the user and the BS  $X_i$ , and  $z > 0$  is the height of  $X_i$ .

In the following, a Nakagami- $m$  fading model is assumed, which means that  $|h_i|^2$  is gamma distributed with a shape parameter  $m$  and a scale parameter  $1/m$ . The CDF of  $|h_i|^2$  is then  $F_{|h_i|^2}(x) = \gamma(m, mx)/\Gamma(m)$  where  $\gamma(\cdot, \cdot)$  is the lower incomplete gamma function and  $\Gamma(\cdot)$  is the gamma function.

The BSs are assumed to employ dynamic BF, and an analysis based on BS databases [42], [43] revealed that BSs implementing dynamic BF have significantly low sidelobes compared to the main lobe. Additionally, the analysis indicated that network providers equip each BS with three similar antenna arrays oriented at  $120^\circ$  intervals, each capable of covering  $120^\circ$ . From these considerations and for the sake of mathematical tractability, the actual antenna array patterns are approximated using a sectorized antenna model. The gain of the antenna array of a generic BS can be expressed as follows:

$$G_t = \begin{cases} G_{\max} & \text{if } |\theta| \leq \omega \\ 0 & \text{if } |\theta| > \omega \end{cases} \quad (5)$$

where  $\theta \in [0; 2\pi[$  is the angle off the boresight direction and  $\omega$  is the beamwidth of main lobe. The serving BS is assumed to estimate the angle of arrival and to adjust its antenna steering orientation accordingly. The model assumes no alignment error. The beams of all the interfering BSs are considered to be randomly oriented with respect to each other, uniformly distributed in  $[0; 2\pi[$ . Consequently, the gains of the interfering BSs in the direction of the user are Bernoulli random variables with probability  $3\omega/(2\pi)$ , which is the probability that the typical user is illuminated by the main lobe of each interfering BS. For notational simplicity,  $G_{\max} = 1$  is normalized, and then we can simplify the notation as  $P_t G_{\max} \rightarrow P_t$ .

The mathematical expressions derived in the following section are defined for a circular area  $\mathcal{B}$  of radius  $\tau$  located in the  $z = 0$  plane and centered on the calculation point. The calculations take an exclusion radius  $r_e \geq 0$  into account, representing a non-publicly accessible area around the BSs. A closest BS association policy is assumed.

Define  $\bar{P}_{r,i} = \bar{P}_{r,i}(r_i^2) = P_t l_i$ . Let  $S_0 = \bar{P}_{r,0} |h_0|^2$  be the useful power received from the serving BS  $X_0$  that is assumed to be the closest to the user and let  $I_0 = \sum_{i \in \Psi \setminus \{X_0\}} \bar{P}_{r,i} G_i |h_i|^2$  be the aggregate interference. Based on these definitions, the SINR conditioned on the distance to the serving BS is given by

$$\text{SINR}_0 = \frac{S_0}{I_0 + \sigma^2} \quad (6)$$

where  $\sigma^2$  is the thermal noise power. In the following, the performance metrics will be derived for the user DL power exposure defined as

$$\mathcal{P} = \sum_{i \in \Psi} \bar{P}_{r,i} G_i |h_i|^2 = S_0 + I_0, \quad (7)$$

which can be converted into a total IPD as

$$\mathcal{S} = \sum_{i \in \Psi} \frac{P_t G_i |h_i|^2}{4\pi (r_i^2 + z^2)^{\alpha/2}} = \frac{\kappa}{4\pi} \mathcal{P} \quad (8)$$

by definition, and, finally, into a root-mean-square electric field strength in V/m as

$$E[\text{V/m}] = \sqrt{120\pi\mathcal{S}}. \quad (9)$$

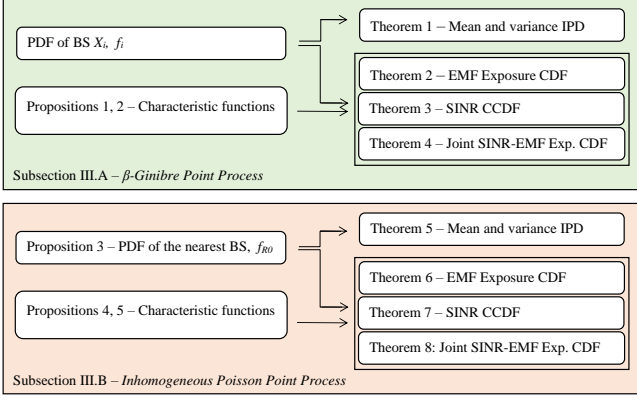


Fig. 1: Organization of Section III

### III. MATHEMATICAL FRAMEWORK

The structure of this section is illustrated in Fig. 1. Let  $T$  be the SINR threshold for reliable transmission at the user equipment, and let  $T'$  be the maximum allowed level of DL EMF exposure in power scale. The CDFs, CCDFs and PDFs can be calculated using Gil-Pelaez's inversion theorem [44] from the knowledge of (i) the characteristic functions (CFs) of the useful signal  $\phi_S$  and of the interference  $\phi_I$ , and (ii) the density function  $f_{R_0, \Theta_0}$  of the position to the serving BS denoted by the random variables  $(R_0, \Theta_0)$ .

#### A. Motion-Invariant Networks: $\beta$ -Ginibre Point Process

Based on the considerations in Subsections II-A and II-B, the mean and the variance of EMF exposure can be calculated.

**Theorem 1.** *The mean of the EMF exposure of a  $\beta$ -GPP given the propagation model in (4) is given by*

$$\mathbb{E}[\mathcal{P}] = \beta \int_{r_e^2}^{\tau^2} \left[ \left( \bar{P}_r(u) + \frac{2p_g c [\bar{P}_r(r^2) (r^2 + z^2)]_{r=\tau}^{r=\sqrt{u}}}{\alpha - 2} \right) \Omega(u) - p_g \beta \int_u^{\tau^2} \Omega^*(u, v) \bar{P}_r(v) dv \right] du \quad (10)$$

where

$$\Omega(u) = \sum_{i \in \mathbb{N}} f_i(u) \Upsilon_i^\beta(u), \quad \Omega^*(u, v) = \sum_{i \in \mathbb{N}} f_i(u) f_i(v) \Upsilon_i^\beta(u),$$

$$\Omega^{**}(u, v, w) = \sum_{i \in \mathbb{N}} f_i(u) f_i(v) f_i(w) \Upsilon_i^\beta(u),$$

$$\Upsilon_i^\beta(u) = \prod_{j \in \mathbb{N} \setminus \{i\}} \left( 1 - \beta + \beta \frac{\Gamma\left(j, \frac{cu}{\beta}, \frac{c\tau^2}{\beta}\right)}{(j-1)!} \right).$$

The associated variance is given by  $\mathbb{V}[\mathcal{P}] = \mathbb{E}[\mathcal{P}^2] - (\mathbb{E}[\mathcal{P}])^2$ , where  $\mathbb{E}[\mathcal{P}^2]$  is given in (11) shown at the top of the next page. We note  $[f(x)]_{x=a}^{x=b} = f(b) - f(a)$ .

*Proof.* The proof of (10) is provided in Appendix A and the proof of (11) is provided in Appendix B.  $\square$

The mean has the same expression as for a PPP, as obtained in [1] without and [30] with dynamic BF. The expressions of

the mean and the variance of the EMF exposure are given for a network of BSs not employing dynamic BF as Corollary 1.

**Corollary 1.** *The mean and the variance of the EMF exposure of a  $\beta$ -GPP when no dynamic BF is employed are respectively given by*

$$\mathbb{E}[\mathcal{P}^*] = \frac{2}{\alpha - 2} c \left[ \bar{P}_r(r) (r^2 + z^2) \right]_{r=\tau}^{r=r_e} \quad (15)$$

and  $\mathbb{V}[\mathcal{P}^*] = \mathbb{E}[\mathcal{P}^{*2}] - (\mathbb{E}[\mathcal{P}^*])^2$ , where  $\mathbb{E}[\mathcal{P}^{*2}]$  is given in (12) shown at the top of the next page.

*Proof.* The proof of (15) is provided at the end of Appendix A and the proof of (12) is provided at the end of Appendix B.  $\square$

The calculation of the higher-order moments of the EMF exposure and the moments of the interference or SINR can be obtained similarly. The CFs of the interference and EMF exposure are provided in Proposition 1 and Corollary 2.

**Proposition 1.** *The CF of the interference of a  $\beta$ -GPP for the propagation model in (4), conditioned on the BS  $X_i$  located at a distance  $r_i = |X_i|$  is*

$$\Phi_{I,i}(q|u) = \prod_{\substack{k \in \mathbb{N} \\ k \neq i}} \left[ \int_u^{\tau^2} f_k(v) \frac{p_g \beta}{(1 - jq \bar{P}_r(v)/m)^m} dv + 1 - p_g \beta \right].$$

*Proof.* The proof is provided in Appendix C.  $\square$

It is worth noting that from the Cauchy-Schwarz theorem and from the definition of a PDF, the integral is always smaller than  $\beta$ , proving that the infinite product converges. To mitigate numerical inaccuracies, the product can be truncated to the  $N$ th term. The impact of such truncation will be analyzed in Section IV-A.

Based on this proposition, the CDF of the EMF exposure, the CCDF of the coverage and the joint CDF of the EMF exposure and SINR are provided in Theorems 2, 3 and 4, respectively.

**Theorem 2.** *The CDF of the EMF exposure of a  $\beta$ -GPP for the propagation model in (4) is given by*

$$F_{emf}(T') \triangleq \mathbb{P}[\mathcal{P} < T'] = \int_{r_e^2}^{\tau^2} \left( \frac{\Omega(u)}{2} - \int_0^\infty \text{Im} \left[ \sum_{i \in \mathbb{N}} f_i(u) \Upsilon_i^\beta(u) \phi_{E,i}(q|u) \frac{e^{-jqT'}}{\pi q} \right] dq \right) du.$$

where  $\phi_{E,i}(q|u) = \Phi_S(q|u) \Phi_{I,i}(q|u)$  and

$$\Phi_S(q|u) = \mathbb{E}_{|h|} [\exp(jqS(u))] = (1 - jq \bar{P}_r(u)/m)^{-m}.$$

*Proof.* The proof is provided in Appendix D.  $\square$

It is noteworthy that, although Gil-Pelaez's theorem is widely applied in SG, it may not be easy to be computed numerically. This originates from the highly oscillatory integrands, particularly caused by the presence of complex exponential functions. To mitigate these challenges, we recommend expressing  $\mathbb{P}[\mathcal{P}/T' < 1]$  instead of  $\mathbb{P}[\mathcal{P} < T']$ . As a result, the inner component of the imaginary part operator can be represented as  $\phi_E(q/T') e^{-jq}$ . In a network of BSs not employing BF, the expression of  $F_{emf}(T')$  simplifies as stated in Corollary 2.

$$\begin{aligned} \mathbb{E} [\mathcal{P}^2] &= \int_{r_e^2}^{\tau^2} \Omega(u) \left( \beta \frac{m+1}{m} \bar{P}_r^2(u) + \beta p_g \bar{P}_r(u) \frac{2c}{\alpha-2} [\bar{P}_r(r^2) (r^2 + z^2)]_{r=\tau}^{r=\sqrt{u}} + \frac{m+1}{m} \frac{p_g c}{\alpha-1} [\bar{P}_r^2(r^2) (r^2 + z^2)]_{r=\tau}^{r=\sqrt{u}} \right. \\ &\quad \left. - p_g^2 c^2 \int_u^{\tau^2} \int_u^{\tau^2} e^{-\frac{c(v+w)}{\beta}} I_0(2c\sqrt{vw}/\beta) \bar{P}_r(v) \bar{P}_r(w) dw dv + \left( \frac{2p_g c}{\alpha-2} [\bar{P}_r(r^2) (r^2 + z^2)]_{r=\tau}^{r=\sqrt{u}} \right)^2 \right) du \\ &\quad - \int_{r_e^2}^{\tau^2} \int_u^{\tau^2} p_g \beta \bar{P}_r(v) \left[ \Omega^*(u, v) \left( \beta \bar{P}_r(u) + \frac{m+1}{m} \bar{P}_r(v) + \frac{4p_g c}{\alpha-2} [\bar{P}_r(r^2) (r^2 + z^2)]_{r=\tau}^{r=\sqrt{u}} \right) - 2p_g \beta \int_u^{\tau^2} \Omega^{**}(u, v, w) \bar{P}_r(w) dw \right] dv du \end{aligned} \quad (11)$$

$$\mathbb{E} [\mathcal{P}^{*2}] = \frac{2(m+1)}{m(\alpha-1)} [\bar{P}_r^2(r) (r^2 + z^2)]_{r=\tau}^{r=r_e} + \left( \frac{2c}{\alpha-2} [\bar{P}_r(r^2) (r^2 + z^2)]_{r=\tau}^{r=r_e} \right)^2 - c^2 \int_{r_e^2}^{\tau^2} \int_{r_e^2}^{\tau^2} e^{-\frac{c(v+w)}{\beta}} I_0\left(\frac{2c\sqrt{vw}}{\beta}\right) \bar{P}_r(v) \bar{P}_r(w) dw dv \quad (12)$$

$$\begin{aligned} G(T, T') &\triangleq \mathbb{E}_0 \left[ \mathbb{P} \left[ \frac{S_0}{I_0 + \sigma^2} > T, S_0 + I_0 < T' \right] \right] \\ &= \beta \int_{r_e^2}^{\tau^2} \left( \frac{\Omega(u)}{2} F_{|h|^2} \left( \frac{T'}{\bar{P}_r(u)} \right) - \frac{1}{\pi q} \int_0^\infty \text{Im} \left[ \sum_{i \in \mathbb{N}} f_i(u) \Upsilon_i^\beta(u) \phi_{I,i}(q|u) \zeta(T, T', \bar{P}_r(u)) \right] dq \right) du \end{aligned} \quad (13)$$

with

$$\zeta(T, T', \bar{P}_r) = \frac{m^m}{(m-1)!} \frac{\gamma \left( m, \frac{-T''}{\bar{P}_r} \left( m + j \frac{\bar{P}_r}{T} \right) \right)}{(m + j \frac{\bar{P}_r}{T})^m} e^{jq\sigma^2} + \frac{m^m}{(m-1)!} \frac{\Gamma \left( m; \frac{T'(m-jq\bar{P}_r)}{\bar{P}_r}, \frac{T''(m-jq\bar{P}_r)}{\bar{P}_r} \right)}{(m - jq\bar{P}_r)^m} e^{-jqT'}. \quad (14)$$

**Corollary 2.** The CF of the EMF exposure of a  $\beta$ -GPP where no dynamic BF is employed is given by

$$F_{emf}^*(T') = \frac{1}{2} - \int_0^\infty \frac{1}{\pi q} \text{Im} \left[ \phi_E^*(q) e^{-jqT'} \right] dq.$$

where  $\phi_E^*(q) = \Phi_I(q|r_e^2)$  with  $p_g = 1$ .

*Proof.* The proof of the CF is similar to the proof of Proposition 1 in Appendix C except that  $p_g = 1$  and that the summation and product are over  $k \in \mathbb{N}$  instead of  $k \in \mathbb{N} \setminus \{i\}$ . The proof of the CDF is similar to the proof of Theorem 2 in Appendix D except that the index  $i$  of the serving BS can be ignored.  $\square$

**Theorem 3.** The CCDF of the SINR of a  $\beta$ -GPP for the propagation model in (4) is given by

$$\begin{aligned} F_{cov}(T) &\triangleq \mathbb{E}_0 [\mathbb{P} [\text{SINR}_0 > T]] \\ &= \beta \int_{r_e^2}^{\tau^2} \left( \frac{\Omega(u)}{2} + \int_0^\infty \text{Im} \left[ \sum_{i \in \mathbb{N}} f_i(u) \Upsilon_i^\beta(u) \phi_{\text{SINR},i}(q|u) \right] \frac{dq}{\pi q} \right) du \end{aligned}$$

where  $\phi_{\text{SINR},i}(q|u) = \phi_S(q|u) \phi_{I,i}(-Tq|u) e^{-jTq\sigma^2}$ .

*Proof.* The proof is similar to the proof of Theorem 2 in Appendix D. The only differences are that for the CCDF of the SINR,  $F_i(T') = 1 - \mathbb{P}(S_0(i) - TI_0(i) \leq T\sigma^2, \mathcal{A}_i)$  and that  $\phi_{E,i}(q|u)$  must be replaced by  $\phi_{\text{SINR},i}(q|u)$ .  $\square$

In the case of Rayleigh fading, the CCDF of the SINR has been computed in [24] for a GPP and in [23] for a  $\beta$ -GPP. Theorem 3 is more general since it can be applied to other fading distributions, such as the Nakagami- $m$  fading given as an example, and because it includes dynamic BF.

**Theorem 4.** The joint CDF of the EMF exposure and SINR for a  $\beta$ -GPP is given in (13) shown at the top of the page.

*Proof.* The proof is provided in Appendix H.  $\square$

It can be noticed that the conditional distributions of the EMF exposure and coverage can also be calculated from these three CDFs using Bayes' rule.

**B. Motion-Variant Networks: Inhomogeneous Poisson Point Process**

**Proposition 2.** The PDF of the distance from the user located at the origin to the nearest BS, is given by

$$f_{R_0}(r_0) = \frac{\Lambda^{(1)}(r_0) e^{-\Lambda(r_0)}}{e^{-\Lambda(r_e)} - e^{-\Lambda(\tau)}}$$

where

$$\begin{aligned} \Lambda(r) &= 4\tilde{a} \int_0^r |u - \tilde{\rho}|^{-1} K(u) u du + \pi \tilde{b} r^2 \\ &\quad + 4\tilde{c} \int_0^r |u - \tilde{\rho}| E(u) u du + \pi \tilde{d} \left( \frac{r^4}{2} + \tilde{\rho}^2 r^2 \right) \end{aligned} \quad (16)$$

is the intensity measure,

$$\Lambda^{(1)}(r) = 2\pi r \left( \frac{2\tilde{a}K(r)}{\pi|r - \tilde{\rho}|} + \tilde{b} + \frac{2\tilde{c}}{\pi} |r - \tilde{\rho}| E(r) + \tilde{d} (r^2 + \tilde{\rho}^2) \right) \quad (17)$$

is its derivative,

$$K(u) = \int_0^{\pi/2} \frac{1}{\sqrt{1 - k(u) \sin^2 \varphi}} d\varphi = \frac{\pi}{2} {}_2F_1 \left( \frac{1}{2}, \frac{1}{2}, 1; k(u) \right)$$

is the complete elliptic integral of the first kind,

$$E(u) = \int_0^{\pi/2} \sqrt{1 - k(u) \sin^2 \varphi} d\varphi = \frac{\pi}{2} {}_2F_1 \left( \frac{1}{2}, \frac{-1}{2}, 1; k(u) \right),$$

is the complete elliptic integral of the second kind and  $k(u) = -4u \tilde{\rho} (u - \tilde{\rho})^{-2}$ .

*Proof.* From the definition of Poisson's law, it follows that the void probability, i.e., the probability of having 0 BS within a disk of radius  $r_0$  centered at the origin of an infinite network, is  $\exp(-\Lambda(r_0))$  with  $\Lambda$  the intensity measure of the PP. The

$$\begin{aligned} \bar{P}_{I_r}(r_0) = p_g \int_{r_0}^{\tau} \bar{P}_r(r) \Lambda^{(1)}(r) dr = -\frac{2\pi\tilde{d}p_g}{(4-\alpha)(\alpha-2)} \left[ ((\alpha-2)r^2 + 2z^2) \bar{P}_r(r) (r^2 + z^2) \right]_{r=\tau}^{r=r_0} \\ + p_g \left( 2\pi\tilde{b} + 2\pi\tilde{d}\tilde{\rho}^2 \right) \frac{[\bar{P}_r(r) (r^2 + z^2)]_{r=\tau}^{r=r_0}}{\alpha-2} + 4p_g \int_{r_0}^{\tau} \bar{P}_r(r) r \left( \frac{\tilde{a}}{|r-\tilde{\rho}|} K(r) + \tilde{c}|r-\tilde{\rho}|E(r) \right) dr \end{aligned} \quad (18)$$

$$\begin{aligned} \bar{P}_{I_r^2}(r_0) = p_g \frac{m+1}{m(\alpha-1)} \left( \pi\tilde{b} + \pi\tilde{d}\tilde{\rho}^2 \right) [\bar{P}_r^2(r) (r^2 + z^2)]_{r=\tau}^{r=r_0} + 4p_g \frac{m+1}{m} \int_{r_0}^{\tau} \bar{P}_r^2(r) r \left( \frac{\tilde{a}}{|r-\tilde{\rho}|} K(r) + \tilde{c}|r-\tilde{\rho}|E(r) \right) dr \\ - p_g \frac{(m+1)\pi\tilde{d}}{m(\alpha-2)(\alpha-1)} \left[ ((\alpha-1)r^2 + z^2) \bar{P}_r^2(r) (r^2 + z^2) \right]_{r=\tau}^{r=r_0} + p_g^2 \bar{P}_{I_r}^2(r_0). \end{aligned} \quad (19)$$

probability of having the nearest BS at a distance  $r_0$  is then  $1 - \exp(-\Lambda(r_0))$ . The nearest BS being in any case located in a ring of inner radius  $r_e$  and outer radius  $\tau$ , the CDF of the distance to the nearest BS is given by

$$F_{R_0}(r_0) = \frac{e^{-\Lambda(r_0)}}{e^{-\Lambda(r_e)} - e^{-\Lambda(\tau)}}$$

so that the integration over the ring gives 1. Proposition 2 is then obtained by differentiating this CDF with respect to  $r_0$ . The intensity measure is obtained from (3).  $\square$

We calculate hereafter the mean and the variance of the EMF exposure.

**Theorem 5.** *The mean of the EMF exposure for an I-PPP network with the intensity measure in (16) for the propagation model in (4) is given by*

$$\mathbb{E}[\mathcal{P}] = \int_{r_e}^{\tau} (\bar{P}_r(r_0) + \bar{P}_{I_r}(r_0)) f_{R_0}(r_0) dr_0$$

where  $\bar{P}_{I_r}(r_0)$  is given in (18) shown at the top of the page. The associated variance is given by  $\mathbb{V}[\mathcal{P}] = \mathbb{E}[\mathcal{P}^2] - (\mathbb{E}[\mathcal{P}])^2$ , where  $\mathbb{E}[\mathcal{P}^2]$  is given by

$$\mathbb{E}[\mathcal{P}^2] = \int_{r_e}^{\tau} \left( \frac{m+1}{m} \bar{P}_r^2(r_0) + \bar{P}_r(r_0)\bar{P}_{I_r}(r_0) + \bar{P}_{I_r^2}(r_0) \right) f_{R_0}(r_0) dr_0 \quad (20)$$

with  $\bar{P}_{I_r^2}(r_0)$  given in (19) shown at the top of the page.

*Proof.* The proof is provided in Appendix E.  $\square$

**Corollary 3.** *The mean of the EMF exposure for an I-PPP network with the intensity measure in (16) when no dynamic BF is employed is given by  $\mathbb{E}[\mathcal{P}^*] = \bar{P}_{I_r}(r_e)$  with  $p_g = 1$ . The associated variance is given by  $\mathbb{V}[\mathcal{P}^*] = \mathbb{E}[\mathcal{P}^{*2}] - (\mathbb{E}[\mathcal{P}^*])^2$ , where  $\mathbb{E}[\mathcal{P}^{*2}]$  is given by  $\bar{P}_{I_r^2}(r_e)$ .*

*Proof.* If no dynamic BF is used, there is no need to analyze the terms  $S_0$  and  $I_0$  separately. Campbell's theorem can therefore be applied to the sum  $S_0 + I_0$ .  $\square$

The calculation of the higher-order moments of the EMF exposure and the moments of the interference or SINR can be obtained similarly. The CF of the interference is provided in Proposition 3.

**Proposition 3.** *The CF of the interference for an I-PPP with the intensity measure in (16) for the propagation model in (4), conditioned on the distance between the typical user at the*

*origin and the nearest BS, is given in (21) shown at the top of the next page.*

*Proof.* The proof is provided in Appendix G.  $\square$

Based on these propositions, the CDF of the EMF exposure, the CCDF of the coverage and the joint CDF are provided as Theorems 6, 7 and 8, respectively.

**Theorem 6.** *The CDF of the EMF exposure for an I-PPP with the intensity measure in (16) for the propagation model in (4) is*

$$\begin{aligned} F_{emf}(T') &\triangleq \mathbb{P}[\mathcal{P} < T'] \\ &= \int_{r_0}^{\tau} \left( \frac{1}{2} - \int_0^{\infty} \frac{1}{\pi q} \text{Im} \left[ \phi_E(q|r_0) e^{-jqT'} \right] dq \right) f_{R_0}(r_0) dr_0 \end{aligned}$$

where  $\phi_E(q|r_0) = \Phi_S(q|r_0) \Phi_I(q|r_0)$  and

$$\phi_S(q|r_0) = \mathbb{E}_{|h|^2} [\exp(jqS_0)] = (1 - jq\bar{P}_{r,0}/m)^{-m}.$$

*Proof.* The proof follows from Gil-Pelaez's theorem.  $\square$

In a network of BSs not employing BF, the expression of  $F_{emf}(T')$  simplifies as stated in Corollary 4.

**Corollary 4.** *The CF of the EMF exposure of an IPPP where no dynamic BF is employed is given by*

$$F_{emf}^*(T') = \frac{1}{2} - \int_0^{\infty} \frac{1}{\pi q} \text{Im} \left[ \phi_E^*(q) e^{-jqT'} \right] dq.$$

with  $\phi_E^*(q) = \Phi_I(q|r_e^2)$  with  $p_g = 1$ .

**Theorem 7.** *The CCDF of the SINR for an I-PPP with the intensity measure in (16) for the propagation model in (4) is given by*

$$\begin{aligned} F_{cov}(T) &\triangleq \mathbb{E}_0 [\mathbb{P}[\text{SINR}_0 > T]] \\ &= \int_{r_0}^{\tau} \left( \frac{1}{2} + \int_0^{\infty} \text{Im} [\phi_{\text{SINR}}(q, T|r_0)] \frac{1}{\pi q} dq \right) f_{R_0}(r_0) dr_0 \end{aligned}$$

where  $\phi_{\text{SINR}}(q, T|r_0) = \phi_S(q|r_0) \phi_I(-Tq|r_0) \exp(-jTq\sigma^2)$ .

*Proof.* The proof is obtained by applying Gil-Pelaez's theorem and by applying the expectation over the distance to the nearest BS  $R_0$  and over the angle  $\Theta_0$ .  $\square$

**Theorem 8.** *Let  $T'' = T(T' + \sigma^2)/(1 + T)$ . The trade-off between EMF exposure and network coverage for an I-PPP is provided by the joint CDF of the EMF exposure and SINR, given in (22) shown at the top of the next page.*



$$\begin{aligned} \phi_I(q|r_0) = \exp & \left[ 4p_g \int_{r_0}^{\tau} \frac{\tilde{a}|\tilde{\rho} - u|^{-1} K(u) + \tilde{c}|\tilde{\rho} - u| E(u)}{(1 - jq\tilde{P}_r(u)/m)^m} u du - [\Lambda(r)]_{r=r_0}^{r=\tau} \right. \\ & \left. + p_g \left[ \frac{\pi\tilde{d}}{\alpha-2} (r^2 + z^2)^{2-\alpha} {}_2F_1 \left( m, 2 - \frac{4}{\alpha}, 3 - \frac{4}{\alpha}; \frac{jq\tilde{P}_r(r)}{m} \right) + \pi \frac{\tilde{b} + \tilde{d}(\tilde{\rho}^2 - z^2)}{\alpha-1} (r^2 + z^2)^{1-\alpha} {}_2F_1 \left( m, 2 - \frac{2}{\alpha}, 3 - \frac{2}{\alpha}; \frac{jq\tilde{P}_r(r)}{m} \right) \right]_{r=r_0}^{r=\tau} \right] \quad (21) \end{aligned}$$

$$G(T, T') \triangleq \mathbb{E}_0 \left[ \mathbb{P} \left[ \frac{S_0}{I_0 + \sigma^2} > T, S_0 + I_0 < T' \right] \right] = \int_{r_0}^{\tau} \left[ \frac{1}{2} F_{|h|^2} \left( \frac{T'}{\tilde{P}_{r,0}} \right) - \int_0^{\infty} \frac{1}{\pi q} \text{Im} [\phi_I(q|r_0) \zeta(T, T', \tilde{P}_r)] dq \right] f_{R_0}(r_0) dr_0 \quad (22)$$

where  $\zeta(T, T', \tilde{P}_{r,0})$  is given by (14).

*Proof.* The proof is provided in Appendix H.  $\square$

The expression of Theorems 7 and 8 can be simplified because the integral over  $\theta_0$  is equal to  $2\pi$ .

#### IV. NUMERICAL RESULTS

##### A. Motion-Invariant Networks: $\beta$ -Ginibre Point Process

In this section, the performance of a  $\beta$ -GPP network is analyzed based on the system model described in Section II. In order to have a realistic set of parameters, the 5G NR 2100 network of a major network provider in Paris (France) is studied. The BSs located inside a disk of radius  $\tau = 6000$  m and center (652, 6862) km in the Lambert 93 conformal conic projection [45] are considered. The  $\beta$ -GPP with  $\beta = 0.75$  was found to be the best fit for this motion-invariant network by applying the methodology proposed in [22]. The system parameters extracted from the operator's database [42] are given in Table II. The half-power beamwidth of the observed antenna patterns, 0.0982 rad, is taken as the value of  $\omega$ , leading to  $p_g = 0.0469$ . Based on propagation models used in similar urban environments [1], [46], [47], we set the path loss exponent  $\alpha = 3.2$ . The noise power is  $\sigma^2 = 10 \log_{10}(k T_0 B_w) + 30 + \mathcal{F}_{dB}$  in dBm where  $k$  is the Boltzmann constant,  $T_0$  is the standard temperature (290 K),  $B_w$  is the bandwidth and  $\mathcal{F}_{dB}$  = 6 dB is the receiver noise figure [48]. The carrier frequency  $f$  and the bandwidth  $B_w$  correspond to the official band allocated to the operator in DL. Numerical results are presented for Rayleigh fading ( $m = 1$ ), justified by the considered frequency band for non line-of-sight propagation environments.

$f$	2 132.7 MHz	$B_w$	14.8 MHz
$\lambda$	6.17 BS/km <sup>2</sup>	$r_e$	0 m
$\alpha$	3.2	$\tau$	6 km
$P_t G_{max}$	66 dBm	$\beta$	0.75
$z$	33 m	$\sigma^2$	-96.27 dBm
$p_g$	0.0469		

TABLE II: System parameters used for Subsection IV-A

1) *Numerical validation:* The mean EMF exposure is found to be  $1.38 \cdot 10^{-4}$  W/m<sup>2</sup> (0.23 V/m) with a variance of  $3.92 \cdot 10^{-7}$  W<sup>2</sup>/m<sup>4</sup> using Theorem 1, (8) and (9). The value of the mean EMF exposure obtained using  $10^8$  realizations of Monte Carlo (MC) simulations shows a difference of  $2 \cdot 10^{-8}$  W/m<sup>2</sup>, showing that the approximation made in the proof in Appendix A is insignificant. The marginal distributions of the EMF exposure (Theorem 2) and SINR (Theorem 3) are validated in Figs. 2 and 3 via MC simulations. The convergence of

the corresponding expressions is also illustrated as a function of  $N$ , representing the number of terms considered within the summation in  $F_{emf}(T')$  and  $F_{cov}(T)$ . Figs. 2 and 3 illustrate that truncating the infinite sums and products in the equations to  $N = 10$  yields a highly accurate approximation of the CDFs. Extending the truncation to  $N = 50$  results in a maximal absolute error of 0.4% for the CDF of the EMF exposure in the head of the distribution and an absolute error of 0.2% in the CCDF of SINR. The area around the 95th percentile has been magnified in Fig. 2 as it is an important statistical measure for EMF exposure assessment. By way of comparison, the Paris authorities set the maximum cumulative exposure threshold at 5 V/m 900MHz equivalent [49], i.e. 7.44 V/m at 2 132.7 MHz, which corresponds to -6.36 dBm using the conversions (8) and (9). The values of EMF exposure obtained in this section are well below the legal threshold but we draw the reader's attention to the fact that the legal limit corresponds to a cumulative sum of EMF exposure caused by all operators and all cellular frequency bands, whereas this study deals with a single frequency band of a single operator at a time.

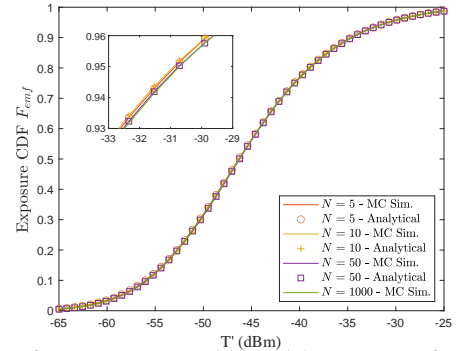


Fig. 2: CDF of EMF exposure with model parameters from Table II

Isocurves depicting the joint CDF of the EMF exposure and SINR are presented in Fig. 4 for various probability values  $p$  such that  $G(T, T') = p$ . Due to the intricate nature of the equations, the analytical computation of  $G(T, T')$  can be time-consuming. To address this, an efficient solution is to determine the Fréchet lower bound (FLB) and the Fréchet upper bound (FUB), which are respectively defined by

$$\text{FLB} = \max(0, F_{\text{cov}}(T) + F_{\text{emf}}(T') - 1) \quad (23)$$

and

$$\text{FUB} = \min(F_{\text{cov}}(T), F_{\text{emf}}(T')). \quad (24)$$



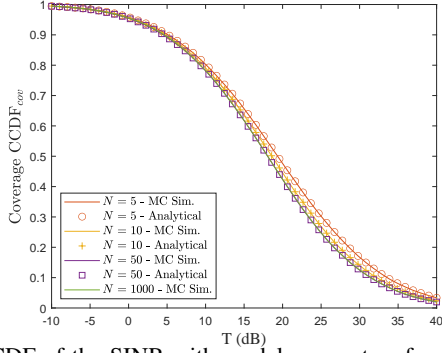


Fig. 3: CCDF of the SINR with model parameters from Table II

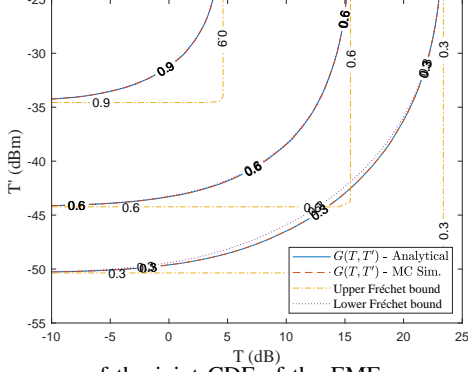


Fig. 4: Isocurves of the joint CDF of the EMF exposure and SINR with the model parameters from Table II.

such that  $FLB \leq G(T, T') \leq FUB$ . Observing Fig. 4, it is evident that the lower bound is close to  $G(T, T')$  and becomes even closer as  $p$  increases. In the pursuit of a conservative analysis, the lower bound can be employed as a substitute for the more intricate expression  $G(T, T')$ .

2) *Impact of the  $\beta$ -parameter:* The marginal distributions of the EMF exposure (Theorem 2) and SINR (Theorem 3) for several values of  $\beta$  are shown in Fig. 5 and 6, respectively. Recalling that the limiting case  $\beta = 0$  corresponds to a H-PPP and  $\beta = 1$  corresponds to a GPP with more regularity, the EMF exposure is lower when the distributions of points is more random while the coverage is improved in networks that are more regularly deployed. This can be explained from three observations. First, in a more regular network, the typical user is on average closer to the serving BS but also to the most interfering BSs, as can be observed from the simulations in Fig. 7. Second, the  $n$ th nearest BS gets closer on average as  $n$  is smaller. Third, the signal power decreases as  $r^{-\alpha}$ . As a consequence, the more regular the network, the greater the power of the useful signal and the greater this latter power in comparison with the power of the interfering signals. To maximize both the coverage and the EMF exposure, the joint CDF of the EMF exposure and SINR can be analyzed.

Isocurves of the joint CDF of the EMF exposure and SINR are shown in Fig. 8 for  $G(T, T') = 0.5$ ,  $G(T, T') = 0.9$  and  $G(T, T') = 0.95$  for a H-PPP, a  $\beta$ -GPP with  $\beta = 0.5$  and a GPP. In general, for a fixed pair  $(T, T')$ , the higher  $\beta$  the better the network performance. For low values of  $T'$ , the trend is opposite. In other words, the benefit of an increase in  $\beta$  in terms of coverage outweighs the negative impact on the exposure, provided that the exposure threshold is not too

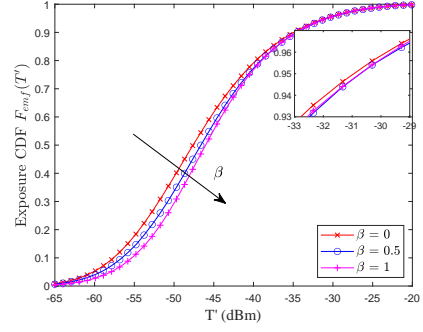


Fig. 5: CDF of the EMF exposure for different values of  $\beta$  in a  $\beta$ -GPP network

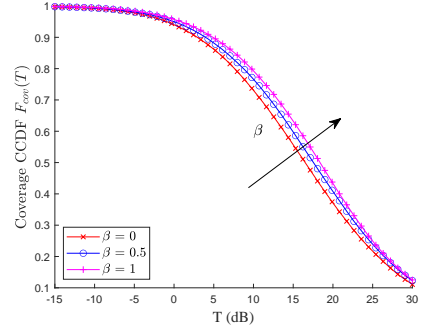


Fig. 6: CCDF of the SINR for different values of  $\beta$  in a  $\beta$ -GPP network

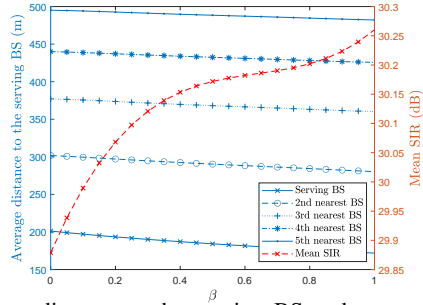


Fig. 7: Average distance to the serving BS and average SINR as a function of  $\beta$

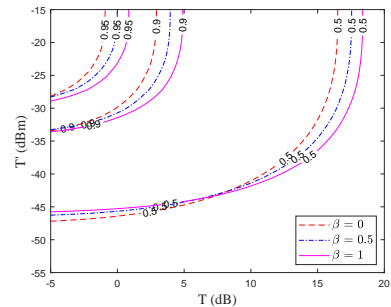


Fig. 8: Isocurves of the joint CDF of the EMF exposure and SINR

low. Figs. 5, 6 and 8 reveal the error made by modeling the Paris network with a simple H-PPP rather than a  $\beta$ -GPP. The Kolmogorov-Smirnov distance between the two, indicating the maximal absolute error, is 7.3% for the CDF of the EMF exposure, 6.1% for the CCDF of the SINR and 7.3% for the joint CDF. These results highlight the importance of an accurate representation of the network topology.

### B. Motion-Variant Networks: Inhomogeneous Poisson Point Process

In this section, we illustrate the results for the I-PPP based on the density model in (2). For illustration, we consider a motion-variant network that corresponds to a cellular network in Brussels, Belgium. At the time of writing, no 5G network has been deployed in Brussels. We decided to use the LTE 1800 BS network of a major telecommunications operator whose data have been extracted from the database [43]. These BSs do not use dynamic BF. The zone under investigation is a disk centered at (797, 7085) km in Lambert 93 projection. It is the origin of the coordinate system in which we do the calculations. In order to cover the whole Brussels-Capital region, the radius of the disk is set at 12 km as can be seen in Fig 9. The fitted parameters and the network parameters are listed in Table III. The central carrier frequency  $f$  and the bandwidth  $B_w$  correspond to the official band allocated to the operator for the DL. Numerical results are presented for Rayleigh fading ( $m=1$ ), justified by the considered frequency band for non line-of-sight propagation environments. In the following, the network performance is calculated for several user locations, using the change of variable explained in Subsection II-A2. The area under investigation is each time a disk with arbitrary radius  $\tau=7$  km, contained in the larger 12 km-radius disk.

$f$	1837.5 MHz	$B_w$	15 MHz
$\alpha$	3.2	$x_0$	-0.145 km
$P_{tG_{max}}$	62.75 dBm	$y_0$	-0.569 km
$z$	33 m	$\tilde{a}$	0.050 km <sup>-1</sup>
$r_e$	0 m	$\tilde{b}$	5.241 km <sup>-2</sup>
$\tau$	7 km	$\tilde{c}$	-0.973 km <sup>-3</sup>
$\sigma^2$	-96.21 dBm	$\tilde{d}$	0.048 km <sup>-4</sup>
$p_g$	1		

TABLE III: System parameters used for subsection IV-A

1) *Impact of the user location in the network:* The metrics of the I-PPP network are calculated at the origin and at (-3 km, -3 km) in the first coordinate system. For each user location, the network area is limited to a disk of radius  $\tau$  centered at the user location. The two disks are illustrated with a red and green border in Fig. 9. Due to the potential time-consuming computation of the mathematical expressions given their complexity, we suggest local approximations using a H-PPP. For each location, the network performance is further compared with two approximations: (a) a H-PPP network with a BS density equal to the average BS density inside a small disk  $\epsilon$  of arbitrary radius 150 m centered at the user location and (b) a H-PPP network with a density equal to the average density inside the 7 km-radius disk centered at the user location. The mathematical expressions of the metrics of these H-PPPs can be obtained by setting  $\tilde{a} = 0 \text{ km}^{-1}$ ,  $\tilde{c} = 0 \text{ km}^{-3}$ ,  $\tilde{d} = 0 \text{ km}^{-4}$  and

$$\tilde{b} = \frac{\int_{\epsilon} \lambda(S) dS}{\int_{\epsilon} dS}.$$

The marginal distribution of the EMF exposure, given by Corollary 4, is displayed in Fig. 10. The solid lines correspond to the results obtained from MC simulations and the markers correspond to values obtained from the mathematical

expressions. The user at the origin of the coordinate system experiences a higher EMF exposure because of its smaller distance to the maximal density ( $x_0, y_0$ ), leading to a higher number of neighboring BSs. The approximation (a) is very good and gets better as the distance from the maximal density increases, contrarily to the approximation (b). This shows that homogenizing the BS density over a very local area gives a good idea of the EMF exposure experienced by the user but when considering large networks, the homogeneity assumption does not hold anymore. The 95th quantile is -34.77 dBm (0.24 V/m) for the user at the origin and -39.34 dBm (0.14 V/m) for the user at (-3 000 m, -3 000 m). The same remarks as for Paris apply when comparing these values to the 14.57 V/m 900MHz equivalent [50] threshold set by the Brussels authorities (i.e. 20.82 V/m at 1 837.5 MHz, corresponding to 2.58 dBm using conversion (8) and (9)). The CCDF of the SINR, given by Theorem 7 and shown in Fig. 11, is on the contrary almost unchanged at the different locations, with only a slight improvement for the user at the origin of the coordinate system.

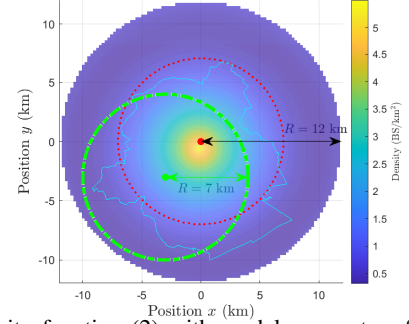


Fig. 9: Density function (2) with model parameters from Table III. The two disks are centered at the two calculation points used in Figs. 10, 11. The borders of the Brussels-Capital region are in light blue.

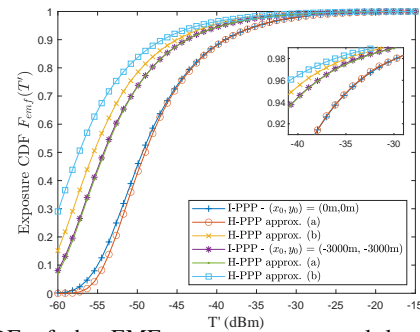


Fig. 10: CDF of the EMF exposure at several locations in the LTE 1800 network of a major Belgian operator in Brussels and comparison with a H-PPP approximation

At last, isocurves of the joint CDF of the EMF exposure and SINR,  $G(T, T') = p$ , given by Theorem 8 are shown in Fig. 12 for  $p = [0.5; 0.95; 0.99]$  and validated via MC simulations.

2) *Overview of the metrics in the network:* In the following, the focus is put on the EMF exposure since it could be concluded from the previous numerical results that the spatial dependence of the coverage is relatively low. The average EMF exposure calculated by Theorem 5 at 2500 locations in the center of Brussels is presented in Fig. 13, and is superimposed

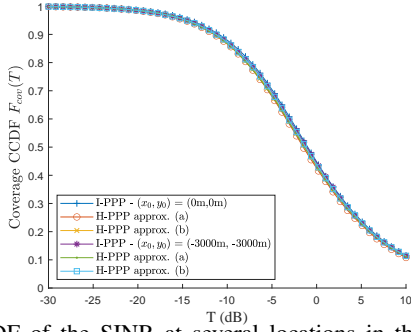


Fig. 11: CCDF of the SINR at several locations in the considered LTE 1800 network and comparison with a H-PPP approximation

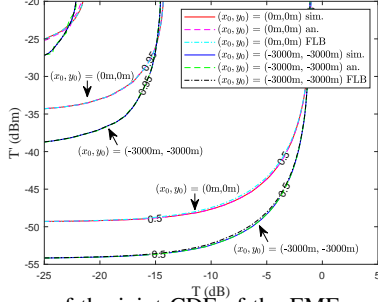


Fig. 12: Isocurves of the joint CDF of the EMF exposure and SINR  $G(T, T') = p$  with  $p = [0.5; 0.95; 0.99]$ . FLB = Fréchet lower bound.

on the Brussels map. As expected, the EMF exposure radially decreases as the distance to the center increases. Statistics of the EMF exposure regardless of the user location are often required. Taking the expected value of the considered network over the two dimensions of space in Theorem 5 gives a value of  $3.50 \cdot 10^{-5} \text{ W/m}^2$  (0.11 V/m).

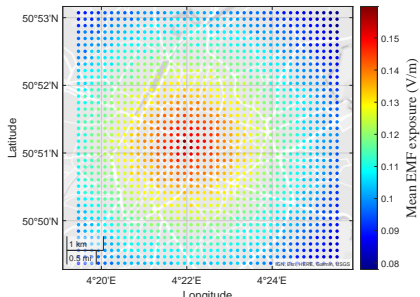


Fig. 13: Mean EMF exposure from the considered LTE 1800 network at 2500 locations in the center of Brussels

The probability to be below the threshold  $T' = -35.7 \text{ dBm}$  (0.22 V/m) is shown at the same 2500 locations in Fig. 14. The relatively low values of the mean EMF exposure compared to the legal threshold leads to choose a relatively low value of  $T'$  for the illustration. Again, taking the expected value of the spatially-dependent CDF of EMF exposure in Theorem 6 provides a CDF of the exposure experienced by any user, regardless of its location, as shown in Fig. 15.

## V. CONCLUSION

In this paper, performance metrics are provided to jointly analyze the EMF exposure and coverage in motion-invariant and motion-variant cellular networks. Based on network

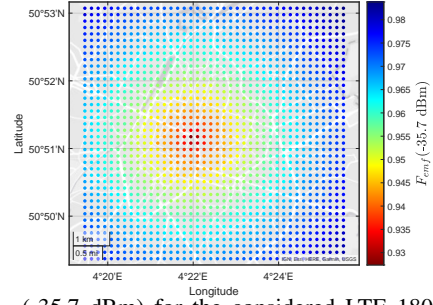


Fig. 14:  $F_{emf}(-35.7 \text{ dBm})$  for the considered LTE 1800 network at 2500 locations in the center of Brussels

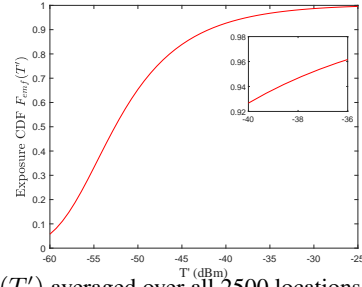


Fig. 15:  $F_{emf}(T')$  averaged over all 2500 locations in the considered LTE 1800 network.

topologies usually encountered in European cities, the  $\beta$ -GPP is used as an example of tractable PP for motion-invariant networks. In motion-variant networks, the network is modeled by an I-PPP. The approach is illustrated for the 5G NR 2100 network in Paris (France) and a LTE 1800 network in Brussels (Belgium) using realistic network parameters. An analysis of the network parameters is also provided and shows that an optimal value of these parameters can be found to maximize the coverage while minimizing the EMF exposure. For future works, performance metrics could be easily adapted for other network models, in other cities, using additional features (more complex BF model, blockage, uplink, heterogeneous cellular networks). The adaptation of the proposed framework to evaluate global EMF exposure, incorporating the correlation between the location of BSs of different technologies and operators, in order to have a faithful way of comparison with the legal thresholds, is another potential avenue for further investigation.

## APPENDIX A

### PROOF OF THE MEAN OF THE EMF EXPOSURE IN A $\beta$ -GPP

As the main beam of the serving BS is assumed to be directed towards the user, while the beams of the interfering BSs are randomly oriented, it is essential to separate the EMF exposure caused by the serving BS and the EMF exposure caused by the interfering BSs. As explained in Subsection II-A1, since each BS can potentially be the serving BS, we have

$$\mathbb{E}[\mathcal{P}] = \mathbb{E}_{\Psi, \xi, |h|, G} \left[ \sum_{i \in \mathbb{N}} \left( \bar{P}_{r,i} G_i |h_i|^2 + \sum_{\substack{j \in \mathbb{N} \\ j \neq i}} \bar{P}_{r,j} G_j |h_j|^2 \xi_j \right) \mathbb{1}_{\xi_i} \mathbb{1}_{\mathcal{A}_i} \right] \quad (25)$$

where  $\mathbb{1}_{\mathcal{A}_i} = \{\mathcal{A}_i = 1\}$  is the indicator function. The expectation operators and the sum over  $i$  can be interchanged. Moreover,  $\Psi$ ,  $\xi$ ,  $|h|$ , and  $G$  are pairwise independent. Given

the model, the normalized gain of the serving BS is  $G_i = 1$ , and  $\mathbb{E}[|h|^2] = 1$ . With these observations and the application of the expectation operators  $\mathbb{E}_\xi$  and  $\mathbb{E}_{G_i}$ , (25) is expressed as

$$\mathbb{E}[\mathcal{P}] = \beta \sum_{i \in \mathbb{N}} \mathbb{E}_{\Psi, \xi} \left[ \left( \bar{P}_{r,i} + \mathbb{E}_G \left[ \sum_{j \in \mathbb{N} \setminus \{i\}} \bar{P}_{r,j} G_j \xi_j \right] \right) \mathbb{1}_{\mathcal{A}_i} \right].$$

The expectation operator  $\mathbb{E}_\Psi$  can be split into the expectation operators  $\mathbb{E}_{|X_i|} = \mathbb{E}_{R_i}$  and  $\mathbb{E}_{\Psi \setminus \{X_i\}}$ . We make a small approximation by applying the expectation operators  $\mathbb{E}_{\Psi \setminus \{X_i\}}$  and  $\mathbb{E}_\xi$  to the sum of the interference and to  $\mathbb{1}_{\mathcal{A}_i}$  independently. The impact of this approximation is shown to be insignificant in the numerical results section. Given that  $\mathbb{E}[\xi_i] = \beta$ , this leads to

$$\begin{aligned} \mathbb{E}[\mathcal{P}] &= \beta \sum_{i \in \mathbb{N}} \mathbb{E}_{R_i} \left[ \left( \bar{P}_{r,i} + \beta \mathbb{E}_{G, \Psi \setminus \{X_i\}} \left[ \sum_{j \in \mathbb{N} \setminus \{i\}} \bar{P}_{r,j} G_j \right] \right) \right. \\ &\quad \times \underbrace{\mathbb{E}_{\Psi \setminus \{X_i\}} \left[ \prod_{j \in \mathbb{N} \setminus \{i\}} \mathbb{E}_{\xi_j} [\mathbb{1}_{\{\xi_j=1, |X_j| > |X_i|\} \cup \{\xi_j=0\}}] \right]}_{\Upsilon_i^\beta(R_i^2)} \left. \right]. \quad (26) \end{aligned}$$

Focusing first on  $\Upsilon_i^\beta(R_i^2)$ , upon applying the expectation operators, the resulting expression is obtained:

$$\Upsilon_i^\beta(R_i^2) = \prod_{j \in \mathbb{N} \setminus \{i\}} \left( \beta \mathbb{E}_{R_j} [\mathbb{1}_{\{R_j^2 > R_i^2\}}] + 1 - \beta \right). \quad (27)$$

Then using the PDF in (1) for the inner expectation results in

$$\mathbb{E}_{R_j} [\mathbb{1}_{\{R_j^2 > R_i^2\}}] = \int_{r_e^2}^{\tau^2} \mathbb{1}_{\{v > R_i^2\}} \frac{v^{j-1} e^{-\frac{cv}{\beta}}}{(j-1)! (\beta/c)^j} dv. \quad (28)$$

Using the generalized incomplete gamma function  $\Gamma(z; a, b) = \int_a^b t^{j-1} e^{-t} dt$  and replacing (28) in (27) leads to

$$\Upsilon_i^\beta(R_i^2) = \prod_{j \in \mathbb{N} \setminus \{i\}} \left( 1 - \beta + \beta \frac{\Gamma\left(j, \frac{cR_i^2}{\beta}, \frac{c\tau^2}{\beta}\right)}{(j-1)!} \right). \quad (29)$$

Then in (26), the sum over  $j$ , excluding the index  $i$ , can be rewritten as the difference between the sum over  $j$  and the term with index  $i$ . As  $\mathbb{E}_G[G] = p_g$  and as the  $G_i$ 's are pairwise independent, by using again the PDF in (1), we have

$$\begin{aligned} \mathbb{E}_{G, \Psi \setminus \{X_i\}} \left[ \sum_{j \in \mathbb{N} \setminus \{i\}} \bar{P}_{r,j} G_j \right] &= \mathbb{E}_{G, \Psi} \left[ \sum_{j \in \mathbb{N}} \bar{P}_{r,j} G_j - \bar{P}_{r,i} G_i \right] \\ &= p_g \int_{R_i^2}^{\tau^2} \left( \sum_{j \in \mathbb{N}} \frac{(\frac{c}{\beta})^j v^{j-1} e^{-\frac{cv}{\beta}}}{(j-1)!} - \frac{(\frac{c}{\beta})^i v^{i-1} e^{-\frac{cv}{\beta}}}{(i-1)!} \right) \bar{P}_r(v) dv. \end{aligned} \quad (30)$$

The sum inside the integral converges and gives

$$\sum_{j \in \mathbb{N}} \frac{v^{j-1}}{(\beta/c)^j (j-1)!} = \sum_{j \in \mathbb{N}_0} \frac{v^j}{(\beta/c)^{j+1} j!} = \frac{c}{\beta} e^{vc/\beta}. \quad (31)$$

Replacing (31) in (30) gives

$$\begin{aligned} \mathbb{E}_{G, \Psi \setminus \{X_i\}} \left[ \sum_{j \in \mathbb{N} \setminus \{i\}} \bar{P}_{r,j} G_j \right] &= \frac{2p_g c/\beta}{\alpha - 2} [\bar{P}_r(r^2) (r^2 + z^2)]_{r=\tau}^{r=R_i} - p_g \int_{R_i^2}^{\tau^2} f_i(v) \bar{P}_r(v) dv. \end{aligned} \quad (32)$$

Replacing (27) and (32) in (26) and applying the expectation operator  $\mathbb{E}_{R_i}$  using (1) leads to

$$\begin{aligned} \mathbb{E}[\mathcal{P}] &= \beta \sum_{i \in \mathbb{N}} \int_{r_e^2}^{\tau^2} \left( \bar{P}_r(u) + \frac{2cp_g}{\alpha - 2} [\bar{P}_r(r^2) (r^2 + z^2)]_{r=\tau}^{r=\sqrt{u}} \right. \\ &\quad \left. - p_g \beta \int_u^{\tau^2} f_i(v) \bar{P}_r(v) dv \right) \times f_i(u) \Upsilon_i^\beta(u) du. \end{aligned}$$

At last, the expression of the mean (10) in Theorem 1 is obtained by switching the sum and the integral, by distributing the product and by defining

$$\Omega(u) = \sum_{i \in \mathbb{N}} f_i(u) \Upsilon_i^\beta(u), \quad \Omega^*(u, v) = \sum_{i \in \mathbb{N}} f_i(u) f_i(v) \Upsilon_i^\beta(u).$$

If no dynamic BF is employed, (25) simplifies to  $\mathbb{E}[\mathcal{P}^*] = \mathbb{E}_{\Psi, |h|, \xi} [\sum_{i \in \mathbb{N}} \bar{P}_{r,i} |h_i|^2 \xi_i]$ . Applying the expectation operators leads to

$$\mathbb{E}[\mathcal{P}^*] = \beta \int_{r_e^2}^{\tau^2} \sum_{i \in \mathbb{N}} \frac{(c/\beta)^i}{(i-1)!} u^{i-1} e^{-cu/\beta} \bar{P}_r(u) du.$$

Repeating step (31) and integrating leads to (10) in Corollary 1.

## APPENDIX B

### PROOF OF THE SECOND MOMENT OF THE EMF EXPOSURE IN A $\beta$ -GPP

Since every BS can potentially be the serving BS, the same reasoning used for the proof of the mean can be applied to derive the second moment of the EMF exposure. By using the result (29), this gives

$$\begin{aligned} \mathbb{E}[\mathcal{P}^2] &= \mathbb{E}[(S_0 + I_0)^2] = \mathbb{E}[S_0^2 + 2S_0 I_0 + I_0^2] \\ &= \mathbb{E} \left[ \sum_{i \in \mathbb{N}} (S_i^2 + 2S_i I_i + I_i^2) \mathbb{P}[X_0 = X_i] \right] \\ &= \sum_{i \in \mathbb{N}} \mathbb{E}_{R_i} \left[ \mathbb{E}_{\Psi \setminus \{X_i\}, G, |h|, \xi} [S_i^2 + 2S_i I_i + I_i^2] \Upsilon_i^\beta(X_i) \right] \end{aligned} \quad (33)$$

We then analyze the the inner expectation operator on each term, separately. Starting with  $\mathbb{E}[S_i^2]$  and knowing that  $\mathbb{E}_{|h|}[|h|^4] = (m+1)/m$ , we have

$$\mathbb{E}_{\Psi \setminus \{X_i\}, G, |h|, \xi} [S_i^2] = \beta \frac{m+1}{m} \bar{P}_{r,i}^2. \quad (34)$$

Now for the cross-term  $\mathbb{E}[S_i I_i]$ , since the  $|h_i|$ 's are pairwise independent, just like the  $\xi_i$ 's and the  $G_i$ 's, we obtain

$$\begin{aligned} \mathbb{E}[S_i I_i] &= \mathbb{E}_{\Psi \setminus \{X_i\}, G, |h|, \xi} \left[ \bar{P}_{r,i} |h_i|^2 G_i \xi_i \sum_{j \in \mathbb{N} \setminus \{i\}} \bar{P}_{r,j} |h_j|^2 G_j \xi_j \right] \\ &= \beta^2 \bar{P}_{r,i} \mathbb{E}_{G, \Psi \setminus \{X_i\}} \left[ \sum_{j \in \mathbb{N} \setminus \{i\}} \bar{P}_{r,j} G_j \right] \end{aligned}$$

Similarly to what is done in (32) for the mean, this gives

$$\begin{aligned} \mathbb{E}[S_i I_i] &= \beta p_g \bar{P}_{r,i} \left( \frac{2c}{\alpha - 2} [\bar{P}_r(r^2) (r^2 + z^2)]_{r=\tau}^{r=R_i} \right. \\ &\quad \left. - \beta \int_{R_i^2}^{\tau^2} f_i(v) \bar{P}_r(v) dv \right). \end{aligned} \quad (35)$$

At last,  $\mathbb{E}[I_i^2]$  can be split into two terms:

$$\mathbb{E}[I_i^2] = \overbrace{\mathbb{E}_{\Psi, G, |h|, \xi} \left[ \sum_{j \in \mathbb{N} \setminus \{i\}} \bar{P}_{r,j}^2 G_j^2 |h_j|^4 \xi_j^2 \right]}^{T_1} + \underbrace{\mathbb{E}_{\Psi, G, |h|, \xi} \left[ \sum_{j \in \mathbb{N} \setminus \{i\}} \sum_{k \in \mathbb{N} \setminus \{i, j\}} \left( \bar{P}_{r,j} G_j |h_j|^2 \xi_j \right) \left( \bar{P}_{r,k} G_k |h_k|^2 \xi_k \right) \right]}_{T_2}$$

By following the same reasoning as before and by using  $\mathbb{E}_G[G^2] = p_g$  for the interfering BSs,  $T_1$  is obtained by

$$\begin{aligned} T_1 &= \beta \frac{m+1}{m} p_g \sum_{j \in \mathbb{N} \setminus \{i\}} \int_{R_i^2}^{\tau^2} f_j(v) \bar{P}_r(v) dv \\ &= \frac{m+1}{m} \frac{p_g c}{\alpha - 1} [\bar{P}_r(r^2) (r^2 + z^2)]_{r=\tau}^{r=R_i} \\ &\quad - \frac{m+1}{m} p_g \beta \int_{R_i^2}^{\tau^2} f_i(v) \bar{P}_r(v) dv \end{aligned} \quad (36)$$

and  $T_2$  is obtained by

$$T_2 = \beta^2 p_g^2 \sum_{j \in \mathbb{N} \setminus \{i\}} \int_{R_i^2}^{\tau^2} f_j(v) \bar{P}_r(v) \sum_{k \in \mathbb{N} \setminus \{i, j\}} \int_{R_i^2}^{\tau^2} f_j(w) \bar{P}_r(w) dw dv.$$

This can be rewritten as

$$\begin{aligned} T_2 &= \beta^2 p_g^2 \underbrace{\left( \sum_{j \in \mathbb{N} \setminus \{i\}} \int_{R_i^2}^{\tau^2} f_j(v) \bar{P}_r(v) dv \right)^2}_{T_{2a}} \\ &\quad - \underbrace{\beta^2 p_g^2 \sum_{j \in \mathbb{N} \setminus \{i\}} \left( \int_{R_i^2}^{\tau^2} f_j(v) \bar{P}_r(v) dv \right)^2}_{T_{2b}} \end{aligned} \quad (37)$$

where  $T_{2a}$  gives

$$\begin{aligned} T_{2a} &= p_g^2 \left( \frac{2c}{\alpha - 2} [\bar{P}_r(r^2) (r^2 + z^2)]_{r=\tau}^{r=R_i} - \beta \int_{R_i^2}^{\tau^2} f_i(v) \bar{P}_r(v) dv \right)^2 \\ &= \left( \frac{2p_g c}{\alpha - 2} [\bar{P}_r(r^2) (r^2 + z^2)]_{r=\tau}^{r=R_i} \right)^2 \\ &\quad - \frac{4p_g^2 c \beta}{\alpha - 2} [\bar{P}_r(r^2) (r^2 + z^2)]_{r=\tau}^{r=R_i} \int_{R_i^2}^{\tau^2} f_i(v) \bar{P}_r(v) dv \\ &\quad + \beta^2 p_g^2 \int_{R_i^2}^{\tau^2} \int_{R_i^2}^{\tau^2} f_i(v) f_i(w) \bar{P}_r(v) \bar{P}_r(w) dw dv \end{aligned} \quad (38)$$

and  $T_{2b}$  can be developed as follows:

$$\begin{aligned} T_{2b} &= p_g^2 \beta^2 \sum_{j \in \mathbb{N}} \int_{R_i^2}^{\tau^2} \int_{R_i^2}^{\tau^2} \frac{(vw)^{j-1} e^{-\frac{c(v+w)}{\beta}} (\frac{c}{\beta})^{2j}}{(j-1)!(j-1)!} \bar{P}_r(v) \bar{P}_r(w) dw dv \\ &\quad - p_g^2 \beta^2 \int_{R_i^2}^{\tau^2} \int_{R_i^2}^{\tau^2} f_i(v) f_i(w) \bar{P}_r(v) \bar{P}_r(w) dw dv \end{aligned}$$

The integrals and the sum in the first line can be switched. The sum over  $j$  converges and gives a modified Bessel function of the first kind  $I_0(x)$  of order 0:

$$\begin{aligned} T_{2b} &= p_g^2 c^2 \int_{R_i^2}^{\tau^2} \int_{R_i^2}^{\tau^2} e^{-\frac{c(v+w)}{\beta}} I_0(2c\sqrt{vw}/\beta) \bar{P}_r(v) \bar{P}_r(w) dw dv \\ &\quad - p_g^2 \beta^2 \int_{R_i^2}^{\tau^2} \int_{R_i^2}^{\tau^2} f_i(v) f_i(w) \bar{P}_r(v) \bar{P}_r(w) dw dv \end{aligned} \quad (39)$$

The second moment in Theorem 1 is given by combining (33), (34), (35), (36), (37), (38) and (39) and by reorganizing the terms.

If no BF is employed, the reasoning is exactly the same as the one to compute  $\mathbb{E}[I_i^2]$ , except that there is no  $j \neq i$  and  $k \neq i$  conditions. There is therefore no summation on the index  $i$  and the only terms that remain are the first term of  $T_1$  in (36), the first term of  $T_{2a}$  in (38) and the first term of  $T_{2b}$  in (39), with the lower bound of the integrals being  $r_e$  instead of  $R_i$ .

## APPENDIX C

### PROOF OF THE CHARACTERISTIC FUNCTION OF THE INTERFERENCE IN A $\beta$ -GPP

From the definition of the CF,

$$\begin{aligned} \Phi_{I,i}(q|R_i^2) &= \mathbb{E} \left[ \exp \left( jq \sum_{k \in \mathbb{N} \setminus \{i\}} \bar{P}_{r,k} |h_k|^2 G_k \xi_k \middle| |X_k| > |X_i| \right) \right] \\ &= \mathbb{E} \left[ \prod_{k \in \mathbb{N} \setminus \{i\}} e^{jq \bar{P}_{r,k} |h_k|^2 G_k \xi_k} \mathbb{1}_{\{|X_k| > |X_i|\}} \right]. \end{aligned}$$

Since the random variables  $\Psi$ ,  $h$  and  $\xi$  are independent,

$$\Phi_{I,i}(q|R_i^2) = \prod_{k \in \mathbb{N} \setminus \{i\}} \mathbb{E}_{\Psi} \left[ \underbrace{\mathbb{E}_{\xi, |h|, G} \left[ e^{jq \bar{P}_{r,k} |h_k|^2 G_k \xi_k} \right]}_{Q(q)} \mathbb{1}_{\{|X_k| > |X_i|\}} \right]. \quad (40)$$

Extracting the term  $Q(q)$  and applying the expectations on  $\xi$  and  $G$  leads to

$$Q(q) = \mathbb{E}_{|h|} \left[ p_g \beta e^{jq \bar{P}_{r,k} |h_k|^2} + 1 - p_g \beta \right].$$

Then for a Nakagami- $m$  fading it becomes

$$Q(q) = \frac{p_g \beta}{(1 - jq \bar{P}_{r,k}/m)^m} + 1 - p_g \beta.$$

Replacing this expression in (40) and applying the expectation on  $\Phi$  using (1) results in Proposition 1.

## APPENDIX D

### PROOF OF THE CDF OF THE EMF EXPOSURE IN A $\beta$ -GPP

Since every BS can be the serving BS,

$$\begin{aligned} F_{\text{emf}}(T') &= \sum_{i \in \mathbb{N}} \mathbb{P}(\mathcal{P} < T', X_0 = X_i) \\ &= \beta \sum_{i \in \mathbb{N}} \underbrace{\mathbb{P}[S_i + I_i < T', \mathcal{A}_i]}_{F_i(T')} \end{aligned} \quad (41)$$

Using Gil-Pelaez' theorem,  $F_i(T')$  can be further expressed as

$$F_i(T') = \mathbb{E}_{\Psi, \xi} \left[ \mathbb{1}_{\mathcal{A}_i} \left( \frac{1}{2} - \int_0^\infty \frac{1}{\pi q} \text{Im} \left[ \phi_{E,i}(q|R_i^2) e^{-jqT'} \right] dq \right) \right]$$

where  $\phi_{E,i}(q|R_i^2) = \Phi_S(q|R_i^2) \Phi_{I,i}(q|R_i^2)$  and

$$\Phi_S(q|R_i^2) = \mathbb{E}_{|h|} [\exp(jqS_i)] = (1 - jq\bar{P}_{r,i}/m)^{-m}.$$

Using the same reasoning as in Appendix A to obtain (26) by using the definition (29) of  $\Upsilon_i^\beta$ , we have

$$F_i(T') = \mathbb{E}_{R_i} \left[ \Upsilon_i^\beta(R_i^2) \left( \frac{1}{2} - \int_0^\infty \frac{1}{\pi q} \text{Im} \left[ \phi_{E,i}(q|R_i^2) e^{-jqT'} \right] dq \right) \right].$$

Applying the expectation operator and using (1) are applied results in

$$F_i(T') = \int_{r_e}^{\tau^2} f_i(u) \Upsilon_i^\beta(u) \left( \frac{1}{2} - \int_0^\infty \frac{1}{\pi q} \text{Im} \left[ \phi_{E,i}(q|u) e^{-jqT'} \right] dq \right) du. \quad (42)$$

Theorem 2 is obtained by replacing (42) in (41).

## APPENDIX E

### PROOF OF THE MEAN EMF EXPOSURE IN AN I-PPP

As the main beam of the serving BS is assumed to be directed towards the user, while the beams of the interfering BSs are randomly oriented, it is essential to separate the EMF exposure caused by the serving BS and the EMF exposure caused by the interfering BSs. The mean EMF exposure can then be written

$$\mathbb{E}[\mathcal{P}] = \mathbb{E}_{\Psi, |h|, G} \left[ \bar{P}_{r,0} G_0 |h_0|^2 + \sum_{i \in \mathbb{N}} \bar{P}_{r,i} G_i |h_i|^2 \right].$$

Using the independence between  $G_i$ ,  $h_i$  and  $\Psi$ , given that  $G_0 = 1$ ,  $\mathbb{E}_G[G_i | i \neq 0] = p_g$  and  $\mathbb{E}_{|h|}[|h_i|^2] = 1$  and using  $\mathbb{E}_\Psi[\cdot] = \mathbb{E}_{X_0}[\cdot] + \mathbb{E}_{\Psi \setminus \{X_0\}}[\cdot]$ , the mean EMF exposure can be further expressed as

$$\mathbb{E}[\mathcal{P}] = \mathbb{E}_{X_0} \left[ \bar{P}_{r,0} + p_g \mathbb{E}_{\Psi \setminus \{X_0\}} \left[ \sum_{i \in \mathbb{N}} \bar{P}_{r,i} \right] \right].$$

It follows from Campbell's theorem that

$$\mathbb{E}[\mathcal{P}] = \mathbb{E}_{X_0} \left[ \bar{P}_{r,0} + p_g \int_{R_0}^{\tau} \bar{P}_r(r) \Lambda^{(1)}(r) dr \right].$$

The mean EMF exposure in Theorem 5 is then obtained by applying Proposition 2 for the expectation over  $X_0$  and by resolving over  $r$ .

## APPENDIX F

### PROOF OF THE SECOND MOMENT OF THE EMF EXPOSURE IN AN I-PPP

The proof is very similar to the proof of a  $\beta$ -GPP in Appendix B. For the reader's convenience, the main steps can be summarized as follows:

$$\mathbb{E}[\mathcal{P}^2] = \mathbb{E}_{X_0} \left[ \mathbb{E}_{|h|} [S_0^2] + 2\mathbb{E}_{\Psi \setminus \{X_0\}, G, |h|} [S_0 I_0] + \mathbb{E}_{\Psi \setminus \{X_0\}, G, |h|} [I_0^2] \right] \quad (43)$$

with

$$\mathbb{E}_{|h|} [S_0^2] = \frac{m+1}{m} \bar{P}_{r,0}^2; \quad (44)$$

$$\mathbb{E}_{\Psi \setminus \{X_0\}, G, |h|} [S_0 I_0] = p_g \bar{P}_{r,0} \mathbb{E}_{\Psi \setminus \{X_0\}} \left[ \sum_{i \in \mathbb{N}} \bar{P}_{r,i} \right] \quad (45)$$

$$= p_g \bar{P}_{r,0} \int_{R_0}^{\tau} \bar{P}_r(r) \Lambda^{(1)}(r) dr;$$

$$\mathbb{E}_{\Psi \setminus \{X_0\}, G, |h|} [I_0^2] = \mathbb{E}_{\Psi \setminus \{X_0\}, G, |h|} \left[ \left( \sum_{i \in \Psi \setminus \{X_0\}} \bar{P}_{r,i} G_i^2 |h_i|^2 \right)^2 \right]$$

$$= \mathbb{E} \left[ \sum_{i \in \mathbb{N}} \bar{P}_{r,i}^2 G_i^2 |h_i|^4 \right] + \mathbb{E} \left[ \sum_{i \in \mathbb{N}} \sum_{j \in \mathbb{N} \setminus \{i\}} \bar{P}_{r,i} \bar{P}_{r,j} |h_i|^2 |h_j|^2 G_i G_j \right] \\ \stackrel{(a)}{=} p_g \frac{m+1}{m} \int_{R_0}^{\tau} \bar{P}_r(r) \Lambda^{(1)}(r) dr + p_g^2 \left( \int_{R_0}^{\tau} \bar{P}_r(r) \Lambda^{(1)}(r) dr \right)^2 \quad (46)$$

Campbell's theorem is again used for the first term on the right-hand side, and the PPP's second-order product density formula is used for the second term in step (a) in (46). The latter is equal to  $(\bar{P}_r^I(r|R_0))^2$ . Replacing (44), (45) and (46) in (43) and applying the expectation operator over  $X_0$  results in (20).

## APPENDIX G

### PROOF OF THE CHARACTERISTIC FUNCTION OF INTERFERENCE IN AN I-PPP

Using the definition of the CF and the probability generating functional, the CF for the interference is

$$\phi_I(q) = \exp \left[ \iint_{\mathcal{B}(r_0, \tau)} \left( \mathbb{E}_{G, |h|} \left[ e^{jq \bar{P}_r(r) G |h|^2} \right] - 1 \right) d\Lambda \right] \quad (47)$$

where  $\mathcal{B}(r_0, \tau) = \mathcal{B}(0, \tau) \setminus \mathcal{B}(0, r_0)$  is a ring centered at 0 with inner radius  $r_0$  and outer radius  $\tau$ . For Nakagami- $m$  fading, we have

$$\mathbb{E}_{G, |h|} \left[ e^{jq \bar{P}_r(r) G |h|^2} \right] = p_g (1 - jq/m)^{-m} + 1 - p_g. \quad (48)$$

Replacing (17) and (48) in (47) and integrating over  $\theta$  gives

$$\phi_I(q|r) = \exp \left[ 2\pi p_g \underbrace{\int_{r_0}^{\tau} \frac{\tilde{b}u + \tilde{d}u\tilde{\rho}^2 + \tilde{d}u^3}{(1 - jq\bar{P}_r(u)/m)^m} du}_{\Xi} \right. \\ \left. + p_g \int_{r_0}^{\tau} \left( 4 \frac{\tilde{a}|\tilde{\rho} - u|^{-1} K(u) + \tilde{c}|\tilde{\rho} - u| E(u)}{(1 - jq\bar{P}_r(u)/m)^m} - \Lambda^{(1)}(u) \right) du \right].$$

By definition,  $\int_{r_0}^{\tau} \Lambda^{(1)}(u) du = \Lambda(\tau) - \Lambda(r_0)$ . Let us now focus on  $\Xi$ . The change of variable  $v \rightarrow (u^2 + z^2)^{-\frac{\alpha}{2}}$  leads to

$$\Xi = - \int_{(r_0^2 + z^2)^{-\frac{\alpha}{2}}}^{(\tau^2 + z^2)^{-\frac{\alpha}{2}}} \frac{(\tilde{b} + \tilde{d}\tilde{\rho}^2) v^{1-\frac{2}{\alpha}} + \tilde{d}v^{1-\frac{4}{\alpha}} - \tilde{d}z^2 v^{1-\frac{2}{\alpha}}}{\alpha (1 - jq P_t \kappa^{-1} v/m)^m} dv.$$

Proposition 3 is obtained by resolving over  $v$  and by using the relationship

$$\int_p^q \frac{x^{1-n}}{(1 - \frac{jsx}{m})^m} dx = \left[ \frac{x^{2-n}}{n-2} {}_2F_1 \left( m, 2-n, 3-n; \frac{jsx}{m} \right) \right]_{x=p}^{x=q}$$

obtained from [51] after a change of variable, with  $n \neq 1$  and  $p, q \geq 0$  and  $(1 - jsx)^m$  having its principal value, leading to

$$\Xi = \left[ \frac{\tilde{d}}{2\alpha-4} (r^2 + z^2)^{2-\alpha} {}_2F_1 \left( m, 2 - \frac{4}{\alpha}, 3 - \frac{4}{\alpha}; \frac{jq\bar{P}_r(r)}{m} \right) \right. \\ \left. + \frac{\tilde{b} + \tilde{d}(\tilde{\rho}^2 - z^2)}{2\alpha-2} (r^2 + z^2)^{1-\alpha} {}_2F_1 \left( m, 2 - \frac{2}{\alpha}, 3 - \frac{2}{\alpha}; \frac{jq\bar{P}_r(r)}{m} \right) \right]_{r=r_0}^{r=\tau}$$

## APPENDIX H

### PROOF OF THE JOINT SINR-EXPOSURE CDF

Using the notations  $S = S_0$  and  $I = I_0$ , the joint metric can be expressed as

$$\begin{aligned} G(T, T') &\triangleq \mathbb{P} \left[ \frac{S}{I + \sigma^2} > T, S + I < T' \right] \\ &= \mathbb{P} \left[ I < \frac{S}{T} - \sigma^2, I < T' - S \right] \\ &= \begin{cases} \mathbb{P} [I < S/T - \sigma^2] & \text{if } S/T - \sigma^2 < T' - S, \\ \mathbb{P} [I < T' - S] & \text{if } T' - S < S/T - \sigma^2. \end{cases} \end{aligned}$$

Rewriting the inequalities, remembering that  $I$  is a positive random variable and introducing  $T'' = T(T' + \sigma^2)/(1 + T)$ ,

$$G(T, T') = \begin{cases} \mathbb{P} [I < S/T - \sigma^2] & \text{if } S < T'', \\ \mathbb{P} [I < T' - S] & \text{if } T'' < S < T', \\ 0 & \text{if } S > T'. \end{cases}$$

Let  $F_I(y|r_0, \theta_0)$  be the CDF of the interference conditioned on the location of the serving BS. Using the definition of  $S$  (6) and by linearity, the last equality can be rewritten as

$$\begin{aligned} G(T, T') &= \mathbb{E}_{r_0, \theta_0} \left[ \underbrace{\int_0^{\frac{T''}{\bar{P}_{r,0}}} F_I \left( \frac{x \bar{P}_{r,0}}{T} - \sigma^2 \middle| r_0, \theta_0 \right) f_{|h|^2}(x) dx}_{T_1} \right. \\ &\quad \left. + \underbrace{\int_{\frac{T'}{\bar{P}_{r,0}}}^{\frac{T''}{\bar{P}_{r,0}}} F_I \left( T' - x \bar{P}_{r,0} \middle| r_0, \theta_0 \right) f_{|h|^2}(x) dx}_{T_2} \right] \end{aligned}$$

Let us develop the term  $T_1$ . The following elements can be replaced in the last expression:

- $f_{|h|^2}(x) = \frac{m^m x^{m-1} e^{-mx}}{\Gamma(m)} u(x)$  where  $u(x)$  is the step function;  $F_{|h|^2}(x) = \frac{\gamma(m, mx)}{\Gamma(m)}$  the corresponding CDF;
- $F_I(y|r_0, \theta_0) = \frac{1}{2} - \frac{1}{\pi} \int_0^\infty \text{Im} [\phi_I(q|r_0, \theta_0) e^{-jqy}] q^{-1} dq$  using Gil-Pelaez inversion theorem.

Then by linearity, by swapping the integrals over  $q$  and  $x$ , and by using the definition of the CDF, we obtain

$$\begin{aligned} T_1 &= \frac{1}{2} F_{|h|^2} \left( \frac{T''}{\bar{P}_{r,0}} \right) \\ &- \int_0^\infty \int_0^{\frac{T''}{\bar{P}_{r,0}}} \text{Im} \left[ \phi_I(q|r_0, \theta_0) e^{-jq \left( \frac{x \bar{P}_{r,0}}{T} - \sigma^2 \right)} \right] \frac{m^m x^{m-1} e^{-mx}}{\Gamma(m) \pi q} dx dq. \end{aligned}$$

By swapping the integral over the real number  $x$  with the imaginary part, we have

$$\begin{aligned} T_1 &= \frac{1}{2} F_{|h|^2} \left( \frac{T''}{\bar{P}_{r,0}} \right) \\ &- \frac{m^m}{\Gamma(m)} \int_0^\infty \text{Im} \left[ \phi_I(q|r_0, \theta_0) \int_0^{\frac{T''}{\bar{P}_{r,0}}} e^{-jq \left( \frac{x \bar{P}_{r,0}}{T} - \sigma^2 \right) - mx} x^{m-1} dx \right] \frac{dq}{\pi q}. \end{aligned}$$

The integral inside the imaginary part is of the form

$$\int_a^b e^{-cx} x^{m-1} dx = \frac{1}{c^m} \Gamma(m; ca, cb) \quad \text{if } m > 0.$$

By evaluating this integral, we obtain

$$\begin{aligned} T_1 &= \frac{1}{2} F_{|h|^2} \left( \frac{T''}{\bar{P}_{r,0}} \right) \\ &- \int_0^\infty \frac{1}{\pi q} \text{Im} [\phi_I(q|r_0, \theta_0) \zeta_1(T, T', l(r_0))] dq \quad (49) \end{aligned}$$

where

$$\zeta_1(T, T', \bar{P}_{r,0}) = \frac{m^m}{(m-1)!} \frac{\gamma \left( m, \frac{T''}{\bar{P}_{r,0}} \left( m + j \frac{q \bar{P}_{r,0}}{T} \right) \right)}{\left( m + j \frac{q \bar{P}_{r,0}}{T} \right)^m} e^{jq\sigma^2}.$$

The same reasoning can be applied to the term  $T_2$ . It leads to

$$\begin{aligned} T_2 &= \frac{1}{2} F_{|h|^2} \left( \frac{T'}{\bar{P}_{r,0}} \right) - \frac{1}{2} F_{|h|^2} \left( \frac{T''}{\bar{P}_{r,0}} \right) \\ &- \int_0^\infty \frac{1}{\pi q} \text{Im} [\phi_I(q|r_0) \zeta_2(T, T', \bar{P}_r)] dq \quad (50) \end{aligned}$$

where

$$\zeta_2(T, T', \bar{P}_{r,0}) = \frac{m^m e^{-jqT'}}{(m-1)!} \frac{\Gamma \left( m; \frac{T'(m-jq\bar{P}_{r,0})}{\bar{P}_{r,0}}, \frac{T''(m-jq\bar{P}_{r,0})}{\bar{P}_{r,0}} \right)}{(m-jq\bar{P}_{r,0})^m}.$$

The joint EMF exposure-SINR distribution conditioned on the distance from the user to the serving BS is obtained by grouping the two terms (49) and (50) and by writing  $\zeta(T, T', l_0) = \zeta_1(T, T', l_0) + \zeta_2(T, T', l_0)$ . This demonstration is used to obtain:

- Theorem 4 by inserting the sum of the expectations over the distance to every BS  $X_i$ , as done in Appendix D.
- Theorem 8 by applying the expectation operator over  $r_0$  and  $\theta_0$ , i.e. using the PDF of the distance from the user to the serving BS (2) (there is no dependence on  $\theta_0$  so the corresponding expectation operator leads to a multiplicative factor  $2\pi$ ).

## REFERENCES

- [1] Q. Gontier, L. Petrillo, F. Rottenberg, F. Horlin, J. Wiart, C. Oestges, and P. De Doncker, "A Stochastic Geometry Approach to EMF Exposure Modeling," *IEEE Access*, vol. 9, pp. 91 777–91 787, 2021.
- [2] M. Al Hajj, S. Wang, L. Thanh Tu, S. Azzi, and J. Wiart, "A Statistical Estimation of 5G Massive MIMO Networks' Exposure Using Stochastic Geometry in mmWave Bands," *Applied Sciences*, vol. 10, no. 23, 2020.
- [3] F. Baccelli, M. Klein, M. Lebourges, and S. A. Zuyev, "Stochastic geometry and architecture of communication networks," *Telecommunication Systems*, vol. 7, pp. 209–227, 1997.
- [4] A. Baddeley, *Spatial Point Processes and their Applications*. Berlin, Heidelberg: Springer Berlin Heidelberg, 2007, pp. 1–75.
- [5] F. Baccelli and B. Błaszczyszyn, "Stochastic Geometry and Wireless Networks: Volume I Theory," *Found. Trends Netw.*, vol. 3, no. 3–4, p. 249–449, mar 2009.
- [6] R. Nasri and A. Jaziri, "Analytical Tractability of Hexagonal Network Model With Random User Location," *IEEE Transactions on Wireless Communications*, vol. 15, no. 5, pp. 3768–3780, 2016.
- [7] M. Haenggi and R. K. Ganti, "Interference in Large Wireless Networks," *Found. Trends Netw.*, vol. 3, no. 2, p. 127–248, feb 2009.
- [8] C.-H. Lee, C.-Y. Shih, and Y.-S. Chen, "Stochastic Geometry Based Models for Modeling Cellular Networks in Urban Areas," *Wirel. Netw.*, vol. 19, no. 6, p. 1063–1072, aug 2013.
- [9] H. ElSawy, A. Sultan-Salem, M.-S. Alouini, and M. Z. Win, "Modeling and Analysis of Cellular Networks Using Stochastic Geometry: A Tutorial," *IEEE Communications Surveys & Tutorials*, vol. 19, no. 1, pp. 167–203, 2017.
- [10] J. G. Andrews, F. Baccelli, and R. K. Ganti, "A Tractable Approach to Coverage and Rate in Cellular Networks," *IEEE Transactions on Communications*, vol. 59, no. 11, pp. 3122–3134, 2011.



- [11] D. B. Taylor, H. S. Dhillon, T. D. Novlan, and J. G. Andrews, "Pairwise interaction processes for modeling cellular network topology," in *2012 IEEE Global Communications Conference (GLOBECOM)*, 2012, pp. 4524–4529.
- [12] I. Flint, H.-B. Kong, N. Privault, P. Wang, and D. Niyato, "Analysis of Heterogeneous Wireless Networks Using Poisson Hard-Core Hole Process," *IEEE Transactions on Wireless Communications*, vol. 16, no. 11, pp. 7152–7167, 2017.
- [13] Y. Hmamouche, M. Benjillali, S. Saoudi, H. Yanikomeroglu, and M. Di Renzo, "New Trends in Stochastic Geometry for Wireless Networks: A Tutorial and Survey," *Proceedings of the IEEE*, Mar. 2021.
- [14] C. Saha, M. Afshang, and H. S. Dhillon, "3GPP-Inspired HetNet Model Using Poisson Cluster Process: Sum-Product Functionals and Downlink Coverage," *IEEE Transactions on Communications*, vol. 66, no. 5, pp. 2219–2234, 2018.
- [15] J. Kibilda, B. Galkin, and L. A. DaSilva, "Modelling Multi-Operator Base Station Deployment Patterns in Cellular Networks," *IEEE Transactions on Mobile Computing*, vol. 15, no. 12, pp. 3087–3099, 2016.
- [16] A. Guo and M. Haenggi, "Spatial Stochastic Models and Metrics for the Structure of Base Stations in Cellular Networks," *Wireless Communications, IEEE Transactions on*, vol. 12, pp. 5800–5812, 11 2013.
- [17] H. Zhang, L. Feng, T. Zheng, and D. K. Sung, "Characterization of base station deployment distribution and coverage in heterogeneous networks," *IET Communications*, vol. 15, no. 6, pp. 850–865, feb 2021.
- [18] H. ElSawy, E. Hossain, and M. Haenggi, "Stochastic Geometry for Modeling, Analysis, and Design of Multi-Tier and Cognitive Cellular Wireless Networks: A Survey," *IEEE Communications Surveys & Tutorials*, vol. 15, no. 3, pp. 996–1019, 2013.
- [19] M. Di Renzo, S. Wang, and X. Xi, "Inhomogeneous Double Thinning—Modeling and Analysis of Cellular Networks by Using Inhomogeneous Poisson Point Processes," *IEEE Transactions on Wireless Communications*, vol. 17, no. 8, pp. 5162–5182, 2018.
- [20] Y. Li, F. Baccelli, H. S. Dhillon, and J. G. Andrews, "Fitting determinantal point processes to macro base station deployments," in *2014 IEEE Global Communications Conference*, 2014, pp. 3641–3646.
- [21] J. S. Gomez, A. Vasseur, A. Vergne, P. Martins, L. Decreusefond, and W. Chen, "A Case Study on Regularity in Cellular Network Deployment," *IEEE Wireless Communications Letters*, vol. 4, no. 4, pp. 421–424, Aug 2015.
- [22] Q. Gontier, C. Tsigros, F. Horlin, J. Wiart, C. Oestges, and P. De Doncker, "Modeling the spatial distributions of macro base stations with homogeneous density: theory and application to real networks," *Proc. Of the European Cooperation in Science and Technology (EURO-COST CA20120 TD(22)0174)*, feb 2022.
- [23] N. Deng, W. Zhou, and M. Haenggi, "The Ginibre Point Process as a Model for Wireless Networks With Repulsion," *IEEE Transactions on Wireless Communications*, vol. 14, 01 2014.
- [24] N. Miyoshi and T. Shirai, "A cellular network model with Ginibre configured base stations," *Advances in Applied Probability*, vol. 46, no. 3, pp. 832–845, 2014.
- [25] Y. Wang, M. Haenggi, and Z. Tan, "The Meta Distribution of the SIR for Cellular Networks With Power Control," *IEEE Transactions on Communications*, vol. 66, no. 4, pp. 1745–1757, 2018.
- [26] T. Bai and R. W. Heath, "Analyzing Uplink SINR and Rate in Massive MIMO Systems Using Stochastic Geometry," *IEEE Transactions on Communications*, vol. 64, no. 11, pp. 4592–4606, 2016.
- [27] R. Li, Z. Zhao, Y. Zhong, C. Qi, and H. Zhang, "The Stochastic Geometry Analyses of Cellular Networks With  $\alpha$ -Stable Self-Similarity," *IEEE Transactions on Communications*, vol. 67, no. 3, pp. 2487–2503, 2019.
- [28] K. Huang, "Mobile ad hoc networks powered by energy harvesting: Battery-level dynamics and spatial throughput," in *2013 IEEE International Conference on Communications (ICC)*, 2013, pp. 3121–3125.
- [29] W. Guo and S. Wang, "Radio-frequency energy harvesting potential: a stochastic analysis," *Transactions on Emerging Telecommunications Technologies*, vol. 24, no. 5, pp. 453–457, 2013.
- [30] N. Deng and M. Haenggi, "Energy Correlation Coefficient in Wirelessly Powered Networks with Energy Beamforming," in *ICC 2021 - IEEE International Conference on Communications*, 2021, pp. 1–6.
- [31] Q. Gontier, L. Petrillo, F. Rottenberg, F. Horlin, J. Wiart, C. Oestges, and P. De Doncker, "Semi-empirical Model of Global Exposure using Stochastic Geometry," in *2021 IEEE International Conference on Communications Workshops (ICC Workshops)*, 2021, pp. 1–5.
- [32] L. Chiaraviglio, S. Turco, G. Bianchi, and N. Blefari-Melazzi, "Cellular network densification increases radio-frequency pollution": True or false?" *IEEE Transactions on Wireless Communications*, vol. 21, no. 4, pp. 2608–2622, 2021.
- [33] M. Matalatala, M. Deruyck, E. Tanghe, S. Goudos, L. Martens, and W. Joseph, "Joint optimization towards power consumption and electromagnetic exposure for Massive MIMO 5G networks," in *2018 IEEE 29th Annual International Symposium on Personal, Indoor and Mobile Radio Communications (PIMRC)*, 2018, pp. 1208–1214.
- [34] S. Shikhantsov, A. Thielens, G. Vermeeren, P. Demeester, L. Martens, G. Torfs, and W. Joseph, "Massive MIMO Propagation Modeling With User-Induced Coupling Effects Using Ray-Tracing and FDTD," *IEEE Journal on Selected Areas in Communications*, vol. 38, no. 9, pp. 1955–1963, 2020.
- [35] M. A. Hajj, S. Wang, and J. Wiart, "Characterization of EMF Exposure in Massive MIMO Antenna Networks with Max-Min Fairness Power Control," in *2022 16th European Conference on Antennas and Propagation (EuCAP)*, 2022, pp. 1–5.
- [36] N. A. Muhammad, N. Seman, N. I. A. Apandi, C. T. Han, Y. Li, and O. Elijah, "Stochastic Geometry Analysis of Electromagnetic Field Exposure in Coexisting Sub-6 GHz and Millimeter Wave Networks," *IEEE Access*, vol. 9, pp. 112780–112791, 2021.
- [37] M. Di Renzo and W. Lu, "System-Level Analysis and Optimization of Cellular Networks With Simultaneous Wireless Information and Power Transfer: Stochastic Geometry Modeling," *IEEE Transactions on Vehicular Technology*, vol. 66, no. 3, pp. 2251–2275, 2017.
- [38] T. Tu Lam, M. Di Renzo, and J. P. Coon, "System-Level Analysis of SWIPT MIMO Cellular Networks," *IEEE Communications Letters*, vol. 20, no. 10, pp. 2011–2014, 2016.
- [39] C. Wiame, S. Demey, L. Vandendorpe, P. De Doncker, and C. Oestges, "Joint Data Rate and EMF Exposure Analysis in Manhattan Environments: Stochastic Geometry and Ray Tracing Approaches," *IEEE Transactions on Vehicular Technology*, vol. 73, no. 1, pp. 894–908, 2024.
- [40] C. Wiame, C. Oestges, and L. Vandendorpe, "Joint data rate and EMF exposure analysis in user-centric cell-free massive MIMO networks," 2023, submitted. [Online]. Available: <https://arxiv.org/abs/2301.11127>
- [41] L. Chen, A. Elzanaty, M. A. Kishk, L. Chiaraviglio, and M.-S. Alouini, "Joint Uplink and Downlink EMF Exposure: Performance Analysis and Design Insights," *IEEE Transactions on Wireless Communications*, 2023.
- [42] ANFR, 2023, cartoradio [Online; accessed 13 December 2023]. Available: <https://www.cartoradio.fr/index.html#/cartographie/all/lonlat/2.323026/48.830108>.
- [43] IBGE, 2023, [Online; accessed 13 December 2023]. Available: <https://geodata.environment.brussels/client/view/3a33e35f-6b64-4b28-bb50-5b4c6b7cb29c>.
- [44] J. Gil-Pelaez, "Note on the inversion theorem," *Biometrika*, vol. 38, no. 3-4, pp. 481–482, 12 1951.
- [45] J. P. Snyder, "Map Projections-A Working Manual (U.S. Geological Survey Professional Paper 1395)," U.S. Government Printing Office, Tech. Rep., 1987.
- [46] S. Ichitsubo, T. Furuno, T. Taga, and R. Kawasaki, "Multipath propagation model for line-of-sight street microcells in urban area," *IEEE Transactions on Vehicular Technology*, vol. 49, no. 2, pp. 422–427, 2000.
- [47] E. Damasso and L. Correia, "COST Action 231: Digital Mobile Radio Towards Future Generation Systems: Final Report," European Commission, Tech. Rep., 1999.
- [48] E. Dahlman, S. Parkvall, and J. Skold, *5G NR: The Next Generation Wireless Access Technology*, 1st ed. USA: Academic Press, Inc., 2018.
- [49] "Charte Relative à la téléphonie mobile," Effective since March 2021. Accessible online: <https://cdn.paris.fr/paris/2021/03/15/c45d9c389d8fdefeef5488aba34187a8.pdf>.
- [50] Région de Bruxelles-Capitale, "Ordonnance relative à la protection de l'environnement contre les éventuels effets nocifs et nuisances provoqués par les radiations non ionisantes," ORD 2014-04-03/16, art. 3, 002. Effective since 10 May 2014. Will be updated in 2023.
- [51] K. Driver and S. Johnston, "An integral representation of some hypergeometric functions," *ETNA. Electronic Transactions on Numerical Analysis [electronic only]*, vol. 25, pp. 115–120, 2006. [Online]. Available: <http://eudml.org/doc/127046>